

**T.C.**

**UNIVERSITY OF TURKISH AERONAUTICAL ASSOCIATION  
SCIENCE AND TECHNOLOGY INSTITUTE**

**PARAMETRIC STUDY OF THE EFFECT OF SWEEP AND WINGLET ON  
HELICOPTER ROTOR BLADE IN HOVERING CONDITION  
USING CFD**

**Ph.D. THESIS**

**Hweda Sharif**

**1303947005**

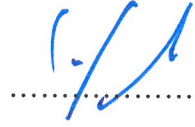
**Thesis Supervisor: Assist. Prof. Dr. Munir Elfarra**

**DEPARTMENT OF MECHANICAL AND AERONAUTICAL  
ENGINEERING**

**DECEMBER 2018**

Hweda Muftah Zaid Sharif, having student number 1303947005 and enrolled in the Ph.D. Program at the Institute of Science and Technology at the University of Turkish Aeronautical Association, after meeting all of the required condition in the related regulations, has successfully accomplished, in front of the jury, the presentation of the thesis prepared with the title of "Parametric Study Of The Effect Of Sweep And Winglet On Helicopter Rotor Blade In Hovering Condition Using CFD".

Thesis Supervisor: Assist. Prof. Dr. Munir ELFARRA  
Ankara Yıldırım Beyazıt University



Jury Members:

Assoc. Prof. Dr. Murat DEMIRAL

University of Turkish Aeronautical Association



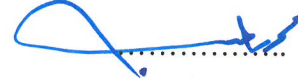
Assist. Prof. Dr. Durmuş Sinan KÖRPE

University of Turkish Aeronautical Association



Assist. Prof. Dr. Mohamed Salem EIMNEFI

University of Turkish Aeronautical Association



Assist. Prof. Dr. Mustafa KAYA

Ankara Yıldırım Beyazıt University



**OF UNIVERSITY OF TURKISH AERONAUTICAL ASSOCIATION  
INSTITUTE OF SCIENCE AND TECHNOLOGY  
STATEMENT NON-PLAGIARISM**

I hereby declare that all information in this study I present as my Ph.D. thesis, entitled “Parametric Study Of The Effect Of Sweep And Winglet On Helicopter Rotor Blade In Hovering Condition Using CFD”, has been presented in accordance with the academic rules and ethical conduct. I also declare and certify with my honor that I have fully cited and referenced all sources utilized in this study.

**28 Dec. 2018.**

**Hweda Muftah Zaid Sharif**



## ABSTRACT

### PARAMETRIC STUDY OF THE EFFECT OF SWEEP AND WINGLET ON HELICOPTER ROTOR BLADE IN HOVERING CONDITION USING CFD

Sharif, Hweda

Ph.D., Department of Mechanical and Aeronautical Engineering

Thesis Supervisor: Assist. Prof. Dr. Munir Elfarra

-2018, 90 pages

The objective of the study is to carry parametric analysis on the effect of different helicopter blade configurations on the rotor performance. The configurations include different sweep angles at different span locations, different winglets and maple shapes. The study was implemented on two different test cases which are, the Caradonna-Tung and UH60A rotor blades. The rotor performance parameters that are studied in this thesis are the thrust, torque and figure of merit. All the computations are obtained using CFD by solving the RANS equations. Three different turbulence models have been used and compared; the Spalart-Allmaras k-epsilon and k-omega SST. The SA has shown the best agreement with measurements at different rotational speeds under different collective pitch angles.

The results of the study shows that, the effect of different sweep angles and locations on the untapered and untwisted Caradonna-Tung (C-T) blade is more that their effect on the twisted UH60A blade. Moreover, the effect on torque was much more pronounced than the effect on thrust. A decrease of around 7 % in torque was possible for the C-T blade while a decreases in torque of around 4% was noticed in the UH60A case. The winglet effect was studied for the UH60A rotor blade and an increase of about 2% in thrust was attained. However, the torque also increases in all the studied cases.

The maple shape resulted in a decrease of almost 5% in torque but also it decreases the thrust.

**Keywords:** Helicopter rotor blade, CFD, Sweep angle, winglet, maple shape, hovering

## ÖZET

### YAŞAM VE KANATLAYIN ETKİSİNİN PARAMETRİK ÇALIŞMASI KONUT DURUMDA HELİKOPTER ROTOR BIÇAKLI CFD KULLANIMI

Çalışma amacı, farklı helikopter bıçak biçimlerinin döneç ( rotor) performansına etkisi üzerine parametrik analiz yapmaktır. Biçimler, farklı kanatçıklar ve akçaağaç şekillerinde farklı tarama açıları içerir. Çalışma, Caradonna – Tung ve UH60A döneç kanatları olmak üzere iki farklı olay üzerinde uygulanmıştır. Bu tezde, üzerinde çalışılan döneç performans parametreleri; itme, tork ve liyakat figürüdür. Tüm hesaplamalar, RANS denklemleri çözülerek CFD kullanılarak elde edilir. Üç farklı türbülans modeli kullanılmış ve karşılaştırılmıştır; Spalart-Allmaras k- epsilon k-omega SST; SA, farklı kolektif açı açılarında farklı dönüş hızlarında yapılan ölçümlerle en iyi uyumu göstermiştir.

Çalışmanın sonuçları, farklı süpürme açılarının konumlarının tempersiz ve bükülmemiş Caradonna- Tung (C-T) bıçağı üzerindeki etkisinin, bükülmüş UH60A bıçağı üzerindeki etkisinden daha fazla olduğunu göstermektedir. Dahası tork üzerindeki etki, itme üzerindeki etkisinden daha belirgindi. C-T bıçağı için torkta yaklaşık % 7 lik bir azalması mümkünken, UH60A olayında, torkta % 4 lük bir azalma fark edildi. Kanat etkisi UH60A döneç bıçağı için çalışıldı ve baskıda yaklaşık % 2 lik bir artış elde edildi. Tork tüm olaylarda artma göstermiştir. Akçaağaç şekli, torkta neredeyse % 5'lik bir azalmayla sonuçlandı, fakat aynı zamanda itişisi de azalttı.

Anahtar kelimeler: helikopter döneç bıçağı, CFD, süpürme, açı, kanatçık akçaağaç şekli, uçmak.

## TABLE OF CONTENTS

ABSTRACT.....	iv
TABLE OF CONTENTS.....	vi
ACKNOWLEDGMENT.....	viii
PUBLICATIONS.....	ix
LIST OF TABLES.....	x
LIST OF FIGURES.....	xii
NOMENCLATURE.....	xv
CHAPTER 1.....	1
INTRODUCTION.....	1
1.2 Literature Survey.....	4
1.3 Objective of the Study.....	9
1.4 Outline of Thesis.....	9
CHAPTER 2.....	11
2.1 Navier-Stokes Equations.....	11
2.2 Reynolds Averaged Navier-Stokes (RANS) Equations.....	14
2.3 Rotation and Velocity Triangle.....	17
2.4 Turbulence Models.....	18
2.5 Boundary Conditions.....	23
2.6 Figure OF Merit (FM).....	25
CHAPTER 3.....	26
VALIDATION STUDY.....	26
3.1 Test Case I: Caradonna –Tung Helicopter Rotor Blade.....	26
3.2 Simulation and Results for Caradonna-Tung Blade.....	29
3.3 Test Case 2: UH-60A Black Hawk Helicopter Blade.....	44
3.4 Simulation and results for UH-60 blade in Hover Condition.....	46

CHAPTER 4 .....	53
PARAMETRIC STUDY .....	53
4.1 Study of Sweep angle and location.....	53
4.2 Winglet Study .....	60
4.3 A Study on Maple-shaped Blade .....	64
CHAPTER 5 .....	67
CONCLUSIONS AND RECOMMENDATIONS.....	67
5.1 Concluding Remarks.....	67
5.2 Recommendations and Future Work .....	68



## ACKNOWLEDGMENT

I am and would always be deeply indebted to my supervisor Assist. Prof. Dr. Munir Elfarrar for his intellectual instructions, encouragement, suggestive ideas, constructive criticism and motivation. His patience and understanding I appreciate helped me sail through the hard times. I am very much grateful on this.

My sincere appreciation and gratitude is extended to my parents, my husband Mabruk and my children (abd al malik and malik ) for their continued support, and patience during my study ☺.

I would also like to express my gratitude and appreciation to my extended family (brothers and sisters) and my friends for their assistance and encouragement I will always remember. I am grateful.

I have been fortunate to befriend many remarkable individuals during my stay at Turkey.



## PUBLICATIONS

Submitted under of Tittle: “*Parametric Study of the Effect of Sweep and Winglet on Helicopter Rotor Blade in Hovering Condition Using CFD*”, (**JOURNAL OF AERONAUTICS AND SPACE TECHNOLOGLES**).



## LIST OF TABLES

Table 4. 1: The percentage of Thrust, Torque and FM for the different cases for rotational speed 2500 rpm .....	56
Table 4. 2: The percentage of Thrust, Torque and FM for the different cases for rotational speed 1750 rpm.....	56
Table 4. 3: The percentage of Thrust, Torque and FM for the different cases for rotational speed 1250 rpm.....	57
Table 4. 4: Optimum Cases for thrust, torque and FM .....	58
Table 4. 5: The percentage of thrust, torque and figure of merit for different cases at the rotational speed 1425rpm.....	60
Table 4. 6: The percentage of Thrust, Torque and Figure of Merit for the different cases at 1425 rpm rotational speed.....	64
Table 4. 7: Compared between untapered and tapered winglet .....	64
Table 4. 8: The percentage of Thrust, Torque and Figure of Merit for the different cases at 1425rpm rotational speed.....	66
Table 3. 1: The real blade of Caradonna-Tung.....	28
Table 3. 2: Different grid system for Caradonna-Tung rotor at 2500 rpm .....	33
Table 3. 3: UH-60A Black Hawk Blade Description for Both the Cases .....	46
Table 3. 4: Twist variations along the UH-60 rotor geometric blade at a high thrust value .....	47
Table 3. 5: Mesh quality of UH-60 Blade.....	48
Table 4. 1: The percentage of Thrust, Torque and FM for the different cases for rotational speed 2500 rpm.....	56

Table 4. 2: The percentage of Thrust, Torque and FM for the different cases for rotational speed 1750 rpm.....	56
Table 4. 3: The percentage of Thrust, Torque and FM for the different cases for rotational speed 1250 rpm.....	57
Table 4. 4: Optimum Cases for thrust, torque and FM .....	58
Table 4. 5: The percentage of thrust, torque and figure of merit for different cases at the rotational speed 1425rpm .....	60
Table 4. 6: The percentage of Thrust, Torque and Figure of Merit for the different cases at 1425 rpm rotational speed.....	64
Table 4. 7: The percentage of Thrust, Torque and Figure of Merit for the different cases at 1425rpm rotational speed.....	<b>Error! Bookmark not defined.</b>

## LIST OF FIGURES

Figure 1. 1: Four forces acting on a helicopter [3].....	1
Figure 1. 2: Hovering Condition [2] .....	2
Figure 1. 3: Forward flight, more lift and thrust [3].....	3
Figure 1. 4: Advancing blade and Retreating blade Side [2] .....	3
Figure 1. 5: Comparison between unswept and swept configuration at hovering flight [9] .....	4
Figure 1. 6: Effect of the sweep angle on the blade performance comparison between BEMT prediction and CFD calculations [12] .....	5
Figure 2. 1: Velocity triangle for a section of the rotor blade.....	17
Figure 3. 1: NACA 0012 Airfoil Geometry.....	27
Figure 3. 2: Caradonna-Tung two-blade model rotor while hovering [31].....	27
Figure 3. 3: Geometry of Caradonna-Tung rotor, [28].....	28
Figure 3. 4:3D Caradonna-Tung blade geometry generated by AutoBlade.....	30
Figure 3. 5:3D view.....	30
Figure 3. 6:(O4H ) grid block structure used.....	31
Figure 3. 7:2D mesh at blade mid-span of Caradonna-Tung rotor.....	33
Figure 3. 8:3D Mesh block structure for Caradonna-Tung rotor.....	34
Figure 3. 9: Pressure coefficient distribution comparison between experimental and CFD calculated at 50%, 80%, 96% span-wise at different mesh levels.....	35
Figure 3. 10:Y+ Value for Caradonna - Tung at 2500 rpm.....	35

Figure 3. 11:Pressure coefficient distribution comparison between experimental and CFD using different turbulence models.....	36
Figure 3. 12;Gauge pressure contours for Caradonna - Tung at 2500 rpm.....	37
Figure 3. 13:Gauge pressure contours for Caradonna - Tung at 1250 rpm.....	38
Figure 3. 14:Gauge pressure contours for Caradonna -Tung at 1750 rpm.....	38
Figure 3. 15: Comparison between Numerical (SA) and experimental at different span-wise sections at 1250 rpm.....	39
Figure 3. 16:Comparison between Numerical (SA) and experimental at different span-wise sections at 1750 rpm.....	40
Figure 3. 17:Comparison of experimental Thrust with different turbulence models Thrust for Caradonna –Tung.....	40
Figure 3. 18:Comparison of sectional lift coefficient for Cardonna-Tung.....	41
Figure 3. 19:Comparison between Numerical (SA) and experimental data at different span-wise sections on Caradonna–Tung at 1250 rpm at 5° collective angle.....	42
Figure 3. 20:Comparison between Numerical (SA) and experimental data at different span-wise sections on Caradonna–Tung at 1750 rpm at 5° collective angle.....	43
Figure 3. 21:Blade and airfoil shape of UH-60A black hawk rotor [63].....	45
Figure 3. 22:The twist distribution of UH-60 blade [60].....	45
Figure 3. 23:3D UH-60A helicopter blade geometry drawn using AutoBlade.....	47
Figure 3. 24:The 2D mesh at blade mid-span of UH-60 helicopter rotor blade.....	48
Figure 3. 25:The 3D mesh for UH-60 helicopter blade.....	49
Figure 3. 26:Y+ Value for UH-60A helicopter.....	49

Figure 3. 27:Comparison between CFD and experimental data at different span-wise sections on UH-60A at 1427 rpm.....	50
Figure 3. 28:Gauge pressure contours for UH-60A blade at 1427 rpm.....	51
Figure 3. 29;Pressure coefficient distribution comparison between the Numerical (SA) and the experimental values at different span-wise sections for UH-60A blade at 1425rpm.....	52
Figure 3. 30:Gauge pressure contours for UH-60A blade at 1425 RPM.....	52
Figure 4. 1: Swept-back blade-tip.....	53
Figure 4. 2: Locational of sweep angle of 40 deg. And 30 deg. At 92% and 94% ....	54
Figure 4. 3: 2D and 3D mesh of 30 degrees and 94%.....	55
Figure 4. 4: Pressure coefficient distribution comparison between Baseline and Optimum Cases at different spanwise sections at 2500rpm and 8 degrees collective pitch angle.....	58
Figure 4. 5: Different sweep angles and sweep locationals of UH-60A.....	59
Figure 4. 6: Different winglet configurations .....	63
Figure 4. 7: Winglet at 80 degrees in case of UH-60A.....	63
Figure 4. 8: Maple shape at 50 degrees.....	65

## NOMENCLATURE

### Letters

$C$	Chord length
$C_D$	Drag coefficient
$C_L$	Lift coefficient
$C_p$	Pressure coefficient
$C_P$	Power coefficient
$C_T$	Thrust coefficient
$e$	Internal energy
$e_0$	Total energy
$\mathbf{F}$	Inviscid flux
$f_{ei}$	External force component
$\mathbf{F}_v$	Viscous flux
$h$	Enthalpy
$h_0$	Total enthalpy
$k$	Coefficient of thermal conductivity, kinetic energy Power
$P$	Power
$p$	Pressure
$Q$	Vector of conservative variables
$q_j$	Heat flux
$r$	Local blade radius
$Re$	Reynolds number
$R$	Radius of blade
$S_T$	Source term
$S_{ij}$	Strain-rate tensor
$t$	Time
$T$	Temperature
$u_i$	Cartesian velocity component
$V$	Space volume
$V_r$	Relative velocity
$V_z$	Axial Velocity
$W_f$	Work performed by external forces

## Greek Letters

$\alpha$	Angle of attack
$\beta$	Twist angle
$\delta_{ij}$	Kronecker delta
$\varepsilon$	Turbulent dissipation
$\theta$	Local pitch angle
$\theta_p$	Pitch angle
$\lambda$	Second coefficient of viscosity, Tip speed ratio
$\mu$	Dynamic viscosity
$\nu$	Kinematic viscosity
$\nu_T$	Turbulent viscosity
$\rho$	Density
$\tau_{ij}$	Viscous stress tensor
$\phi$	Flow angle
$\omega$	Specific turbulent dissipation rate
$\Omega$	Angular speed

## Abbreviations

CFD	Computational Fluid Dynamics
FM	Figure of Merit
RANS	Reynolds Average Navier Stokes
RPM	Revolution Per Minute
SA	Spalart-Allmaras
SST	Shear Stress Transport



## CHAPTER 1

### INTRODUCTION

It has been a challenge for designers and engineers to enhance the aircraft rotor efficiency keeping in view the fact that a rotor faces variations in the flight conditions. Experts have been consistently finding newer and better solutions to this problem. During the previous 15 years, large numbers of experts and researchers have suggested different measures and their aerodynamics effects on a helicopter, which became popular on global level in the wake of growing popularity of helicopters in today's society. Many publications have been published, which discuss the historical development of a rotorcraft [1, 2, 3, 4].

Every helicopter is a rotorcraft, which performs despite facing aerodynamic forces such as weight, thrust, lift and drag. Rotors apply lift and thrust as Figure 1.1 shows. Rotors enable a helicopter to land vertically, take off, hover in the air, and fly vertically, forward or backward. Some studies give comprehensive information on aerodynamics of a helicopter [2-4].

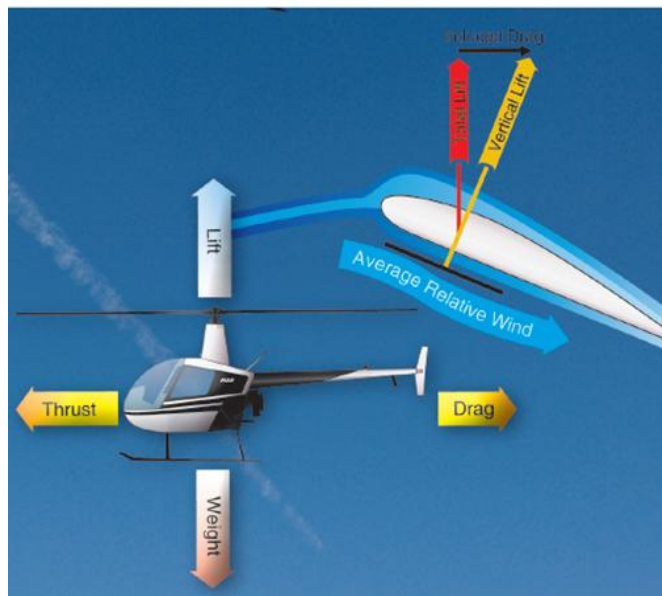


Figure 1. 1: Four forces acting on a helicopter [3]

The requirements of the next generation of rotor aircraft include more payload, range, endurance, and reduction in fuel consumption without compromising advanced features of post-modern rotary-wing vehicles.

These requirements show that the rotor should have maximum available thrust with higher efficiency. Existing rotors are designed to provide balance between forward flight conditions and hovering performance, since hovering is a unique capability of a rotorcraft.

Helicopters can hover in the air at any selected point, which is impossible for aircrafts. The supply lift should be equal to the helicopter's total weight to make hovering possible as Figure 1.2 indicates.

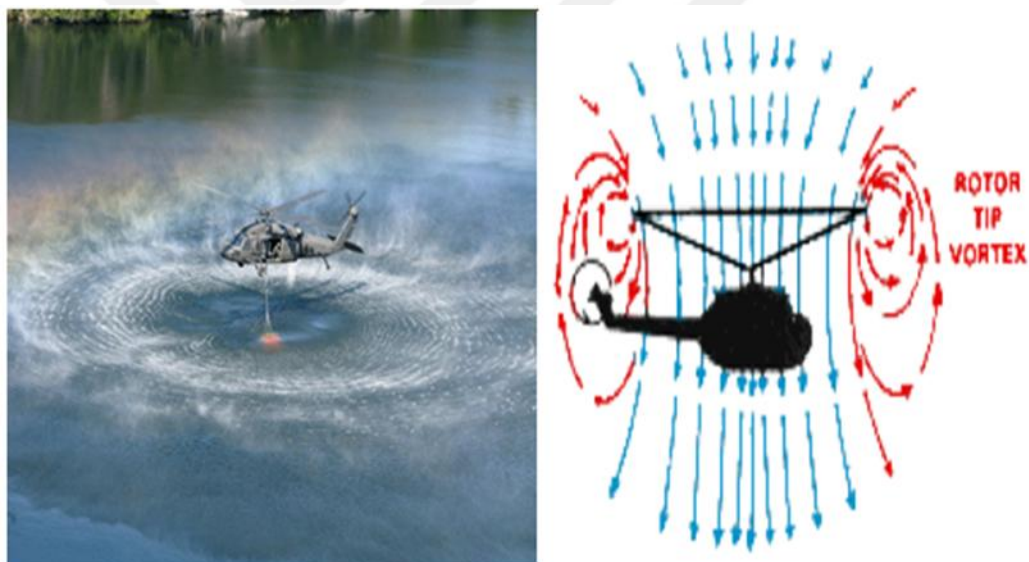


Figure 1. 2: Hovering Condition [2]

Figure 1.3 shows a flight in the forward direction while both air and vertical speeds are constant while weight, lift, drag and thrust should be balanced.

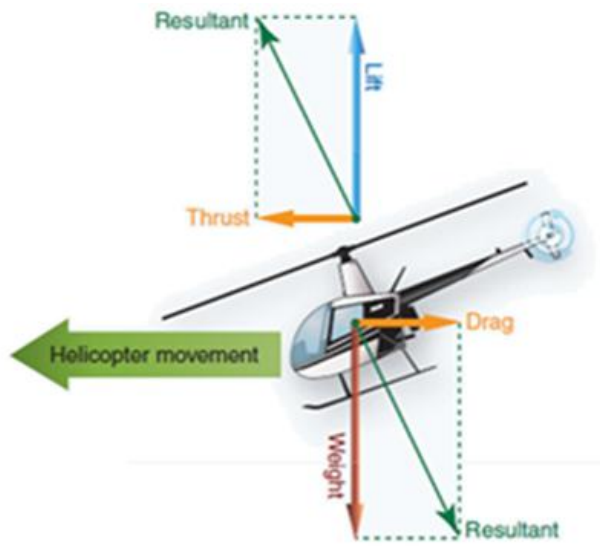


Figure 1. 3: Forward flight, more lift and thrust [3]

Some factors limit rotor efficiency that further limits the forward motion and hovering. For hovering at high altitudes and for taking off, the rotor must provide the maximum lift. On the other hand, a rotor encounters different flow environments while retreating, sideways movements and advancing. The advancing rotor blade moves in the direction of the helicopter while the retreating blade moves in the opposite direction as shown in Figure 1.4.

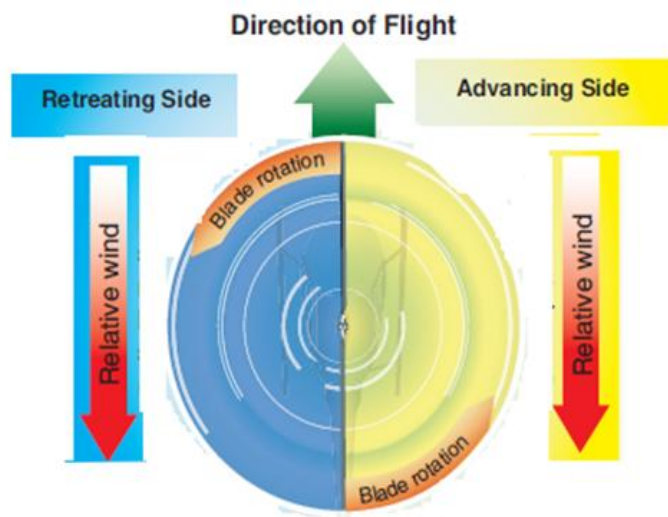


Figure 1. 4: Advancing blade and Retreating blade Side [2]

## 1.2 Literature Survey

The helicopter rotor blades have specific aerodynamic design and geometry that depends on twist distribution, number of blades, sweep function, aerofoil selection and the aerodynamic coefficients.

There are two established approaches, which provide such understanding including, Blade Element Momentum theory (BEM) and Computational Fluid Dynamics (CFD) and Blade Element Momentum Theory BEMT.

### 1.2.1 Blade Element Momentum Theory

BEM is a hybrid process presented by Gustafson and Gessow (1946) and Gessow (1948). It defines the concepts pertaining to blade elements and momentum. The BEM aerodynamics includes a mathematical rotor model that is amalgamation of the simple momentum theory, and the classical blade element theory; therefore, a majority of the sophisticated helicopter rotors are designed according to it. It utilizes 2-D aerofoil analysis and several other mechanical design tools [5, 6].

These analyses sometimes capture the unsteady flow effects through dynamic stall models and the unsteady potential flow theory [7]. Despite simplicity of this aerodynamic model, it shows considerable mathematical parsimoniousness [8], which makes it a reasonable choice for predicting the performances of helicopter rotors, aircraft propellers and prop rotors [9, 10, 11].

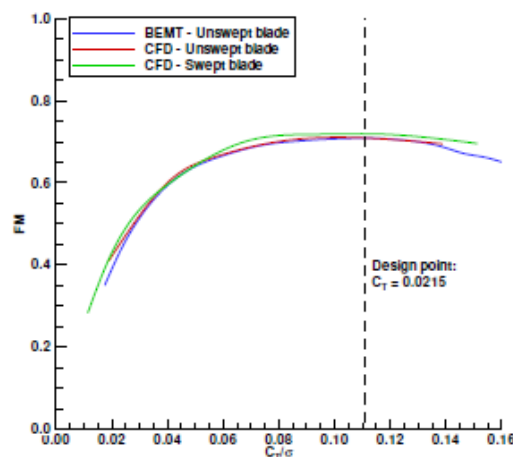
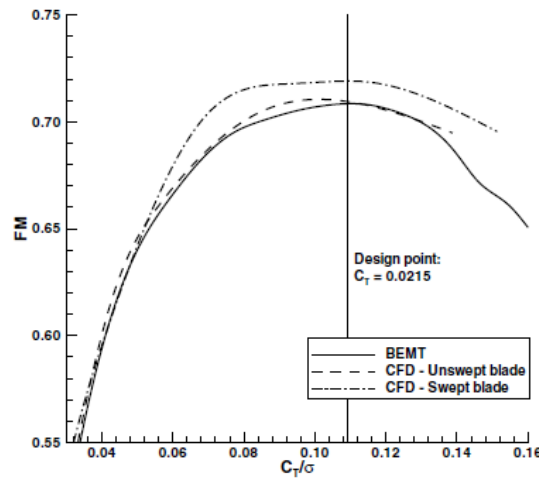


Figure 1. 5: Comparison between unswept and swept configuration at hovering flight [9]

Generally, BEM methods facilitate rotorcraft analysis and design because of their computational efficiency and usefulness. The BEM combined with the genetic algorithm was used during the optimization of a proprotor of a tilt-rotor aircraft [12].



(a) Hover

Figure 1. 6: Effect of the sweep angle on the blade performance comparison between BEMT prediction and CFD calculations [12]

Some researchers applied the momentum theory for experiments on the coaxial rotor performance [13, 14]. Later, [15] the BEM variations in the coaxial rotors showed better comparative results when the coaxial rotor performance was analyzed during a hovering flight, and when highly-twisted blades and their performances were compared [16,17] with the performance of straight/untwisted blades while using basic BEM.

### 1.2.2 Computational Fluid Dynamics; Navier-Stokes Solvers

The Computational Fluid Dynamics (CFD) has been extensively used in advanced aerodynamics that helps analyzing complex flow features. During the recent years, computational methods are increasingly becoming popular for determining the performances of the latest tip designs or CFD. They provide numerical simulations of the fluid flows. This technology has state-of-the-art capabilities, which minimize risk and assure low cost solutions to the existing challenges that aeronautical industry is confronting. However, the main drawback of CFD methods is the high computational time cost. Navier-Stokes solver help finding a direct solution to the governing equations of the flow, and besides, it predicts the correct flow field even without

requiring the airfoil load characteristics. It is applicable to all the helicopter speeds, and it helps predicting 3-D flow characteristics. This process is robust and it has high CPU consumption.

Still, it is difficult to analyze a rotor blade using CFD as compared to utilizing CFD for analyzing fixed wings [18, 26]. T. Alan Egolf and S. Patrick Sparks [18] used mathematical equations in simplified forms including potential flow equations for understanding the flow field of a complicated lifting helicopter rotor.

J. E. Deesef and R. K. Agarwal [19] solved Euler's equations pertaining to the rotating coordinate system based on the blades' body-conforming curvilinear grids, and discussed them during the hovering condition.

The adaptive CFD technique computes rotor-blade aerodynamics. Mustafa et al. have thrown light on it in their study [20]. Mark Potsdam et al. [21] experimented with fluid dynamic code and the rotorcraft computational structural dynamics (CSD) that calculates helicopter rotor air-loads under varying flight conditions.

The Navier-Stokes solver directly solves the governing equations of the flow and correctly predicts the flow fields without requiring characteristics of the airfoil load. It is useful for all the helicopter speeds and it accurately determines/predicts the 3-D flow characteristics. Reynolds-averaged Navier-Stokes (RANS) has been effectively utilized for simulating a helicopter rotors' flow fields both during hovering and forwards flying [22- 25].

A new interface design has been presented to perform as Navier-Stokes flow solver that was applied to assess the isolated-rotor flow fields during hovering conditions.

Terry L. and Thomas H. Conducted this study [22]. Strawn and Ahmad [23] used a RANS solver and OVERFLOW. Pomin and Wagner [24] studied a 7A helicopter rotor blade when it was hovering. They utilized RANS solver using FEM (finite element modelling following Timoshenko beam theory for assessing aero-elastic effects.

Juho Ilkko et al. [25] conducted simulations based on Reynolds-averaged Navier-Stokes equations, which they solved based on the available data of the UH-60A helicopter.

The computations were conducted for validating FINFLO flow solver applying several turbulence models.

Chen et al. developed 3D Euler's solver following the finite volume upwind scheme for calculating the flow fields of the helicopter rotor blade during a forward flight [26]. In conclusion, the CFD was found for simulations, validation and design.

While predicting the wake contraction of a hybrid CFD solver called Helix-1A, a near-body RANS solver is used, which is coupled with a vorticity embedding potential flow solver for the wake flow field [27]. The results were in agreement with experiments. The present study focuses on the effect of parametric factors on the helicopter rotor blade (sweep, winglet and shape of blade) using CFD.

Note: There are some problems in the conventional helicopter blades including lift dissymmetry between the blades, retreating blade stalls, and shock waves, which cause compression.

It studies the effects of sweep, winglet and change in the blade shape from conventional shape into a maple seed shape.

Most of the published works focus on the numerical RANS valuation, simulation and optimization of hovering rotors for different helicopter blades. Such efforts are mentioned in some studies [28-37].

Many studies use Caradonna-Tung rotor blade as a baseline [28-32]. Piotr D and Oskar S [28] have proven that a numerical method implemented in the SPARC code is capable of predicting flow field of a hovering Caradonna-Tung rotor during the transonic conditions.

Hamid F., Ahmad [29] used a latest free-wake CFD process to calculate the aerodynamic loads for two-bladed helicopter rotors during a hovering flight and compared their numerical calculations with the experimental data pertaining to the pressure distribution of the Caradonna-Tung UH-60 blade.

Elfarra M. et al. [30] studied the effect of parabolic chord distribution and the taper stacking point location along the span of a helicopter rotor blade, which was analyzed in terms of the rotor thrust, torque and the figure of merit of the baseline Caradonna-Tung [30].

The rotor hover performance was predicted using CFD methods and simulations for the Helicopter Multi-block (HMB2), and it was validated for the Caradonna and Tung rotor during the hovering position. The overall results show excellent agreement with

the experimental data, which means that the CFD is adequate for resolving the loads and handling the wake structure [32].

During the recent years, M. Imiela and G. Wilke conducted investigations using multi-fidelity approach on various design parameters such as chord, twist, anhedral and sweep. Increase in twist was found at the design point  $C_t / \sigma = 0.093$ , the FM increased by 3.5% in comparison to the baseline rotor [33 and 34], and the best FM shifted in the direction of the higher thrust coefficient.

To create numerical optimization procedures to boost the aerodynamic helicopter rotor performance during the hovering condition, Le Pape and Beaumier [35] modified 7A/7AD rotor's chord distribution, linear aerodynamic twist, sweep, and anhedral distributions, which exhibited reasonable capability to reach new rotor geometries and planforms with high aerodynamic performance.

A study on blade twist geometric modifications shows that certain modification improve a rotorcraft's aerodynamic performance. J.W.Lee and N.A.Vu [34] improved to the airfoil characteristics to a certain range of drag, lift and moment coefficients, which are significant for the performance of a helicopter rotor blade, which increased by 4.3% (0.7 to 0.73).

Researchers conducted a systematic investigation to understand the impact of factors such as anhedral, tip sweep, and planform taper on the rotor blade response; therefore, structural analysis was carried out for loading while a 3D FDA (finite difference aerodynamic) analysis was also conducted [37].

Seokkwan et al. [38] conducted unsteady turbulent flow simulations for investigating the turbulence models and their impact on the predicting efficiency of the isolated XV-15 hovering rotor.

Many previous literature studies used UH-60 helicopter rotor for the research. The validation of its 3D CFD framework was accomplished through comparing the predictions pertaining to a baseline UH-60A rotor with the experimental data. Yashwanth R. [39] tested slatted UH-60A rotor blade with 40% span-slatted airfoil section and a couple of varying slat configurations.

Patrick M. Shinoda [40] evaluated NASA Ames 80x120 feet wind tunnel for hover testing. He compared the rotor performance data with the predicted data, flight data of



UH-60 aircraft and UH-60 model-scale data, and all the data showed good agreement when compared to the full-scale data.

Choi et al. [41] used time-spectral and discrete adjoint-based methods for optimization of UH-60 rotor blade reducing torque without losing thrust.

### 1.3 Objective of the Study

As mentioned before, a helicopter rotor needs maximum power during a hover flight; therefore, it needs a blade design to reduce the power consumption during hovering without compromising the thrust needed for hovering.

The main objective behind this thesis is to run a parametric study on a helicopter blade by changing the sweep angle, adding different winglets and changing the shape into a maple-shaped blade using CFD and see their effects on the blade performance. The following steps were conducted:

- For validation or simulation, two test cases were analyzed; Caradonna-Tung and UH-60A black hawk helicopter rotors were chosen to validate the CFD software used.
- Study the sweep angle and location effect in case of Caradonna-Tung blade (untwisted and untapered) at different rotation speeds.
- Study the effect of sweep angle, sweep location, winglet and maple shape on thrust increase and torque reduction during the hovering conditions for the twisted and tapered UH-60A black hawk helicopter blade.

### 1.4 Outline of Thesis

This thesis has five chapters.

**Chapter 2:** Governing equations and numerical processes applied for simulation are given in this chapter, which also describes many turbulence models applied for the RANS solver. The boundary conditions are also described in this chapter.

**Chapter 3:** Two test cases are taken, investigated, simulated and analyzed in this chapter. The Caradonna-Tung as well as UH-60A Black Hawk was observed

during the hovering flight. The outcomes were compared with the results obtained after experiments, and turbulence models were applied. This chapter validates the solver and hence throws light on the credibility of the whole study. It shows how a suitable turbulence model was chosen for simulations.

**Chapter 4:** Different winglets, sweep angles, locations and configurations were studied for both Caradonna-Tung and UH-60A Black Hawk, and their effects on the thrust output and figure of merit of the helicopter were investigated during the hovering state and mentioned in this chapter.

**Chapter 5:** This chapter includes concluding remarks as well as recommendations for further research.

## CHAPTER 2

### METHODOLOGY

The Computational Fluid Dynamics (CFD) acts as a powerful tool to analyze both existing and new rotorcraft or helicopter configurations, and it is used for detailed flow visualization and performance prediction studies around such configurations. Before using a CFD solver to analyze a new configuration, it should be validated in the light of existing experimental studies for establishing confidence in the predicted values. Since CFD helps understanding the local flow field, the wake is necessary for accurately computing the induced drag. This chapter explains the details regarding the CFD solution methodology used for validation and parametric study.

#### 2.1 Navier-Stokes Equations

In this case, the governing equations represent conservation of mass, momentum and energy. Since basically, the Navier-Stokes equations discuss turbulent as well as laminar flows. The engineering devices such as compressors and wind turbines have prevalent turbulent flows, which require simulation [42].

This chapter describes the numerical processes chosen and applied in the thesis. Navier-Stokes equations are explained first, after which, RANS equations are given. Later, the turbulence models and boundary conditions are mentioned and explained.

The standard 3D Navier-Stokes equation for a surface-bound space volume is as follows:

$$\frac{\partial}{\partial t} \int_V Q dV + \oint_S (F \cdot n) dS - \oint_S (F_v \cdot n) dS = \int_V S_T dV \quad (2.1)$$

Where:

Q Is the vector of conservative variables given by?

$$Q = \begin{Bmatrix} \rho \\ \rho u_1 \\ \rho u_2 \\ \rho u_3 \\ \rho e_0 \end{Bmatrix} \quad (2.2)$$

In the above mentioned vector  $\rho$ ,  $u_i$  and  $e_o$  represent density, Cartesian velocity component, and total energy respectively.

$F$  represents invicid flux while  $F_v$  represents viscous flux, which are given below:

$$F_j = \begin{pmatrix} \rho u_j \\ \rho u_1 u_j + p \delta_{1j} \\ \rho u_2 u_j + p \delta_{2j} \\ \rho u_3 u_j + p \delta_{3j} \\ \rho h_0 u_j \end{pmatrix}, \quad F_{vj} = \begin{pmatrix} 0 \\ \tau_{1j} \\ \tau_{2j} \\ \tau_{3j} \\ u_i \tau_{ij} - q_j \end{pmatrix} \quad (2.3)$$

Here, index,  $j = 1, 2, 3$  are coordinate components while  $P$  and  $h_0$  represent pressure and the total enthalpy respectively.

$S_T$  consists of the source terms defined by:

$$S_T = \begin{pmatrix} \rho \\ \rho f_{e1} \\ \rho f_{e2} \\ \rho f_{e3} \\ W_f \end{pmatrix} \quad (2.4)$$

Where:  $f_{e1}$ ,  $f_{e2}$  and  $f_{e3}$  are external force components and  $W_f$  is the work performed by the mentioned external forces.

$$W_f = \rho f_e \cdot u \quad (2.5)$$

The total enthalpy  $h_0$  is as follows

$$h_0 = e_0 + \frac{p}{\rho} \quad (2.6)$$

Total energy  $e_o$  is as follows

$$e_0 = e + \frac{1}{2} u_i u_i \quad (2.7)$$

Consequently

$$h_0 = h + \frac{1}{2} u_i u_i \quad \text{And} \quad h = e + \frac{p}{\rho} \quad (2.8)$$

In this case,  $e$  represents internal energy while  $h$  shows enthalpy.

Heat flux  $q_j$  is given in the energy equation (Eq. 2.3) with the help of thermal conduction according to the Fourier's Law:

$$q_j = -K \frac{dT}{dx_j} \quad (2.9)$$

Here  $K$  is the thermal conductivity coefficient while  $T$  represents temperature. As for Newtonian fluid, viscous stress tensor  $\tau_{ij}$  in Eq.(2.3) will be:

$$\tau_{ij} = 2\mu S_{ij} + \lambda \frac{\partial u_k}{\partial x_k} \delta_{ij} \quad (2.10)$$

Where:

$\mu$  : Dynamic viscosity.

$\lambda$  : Second coefficient of viscosity.

$\delta_{ij}$  : Kronecker delta and  $S_{ij}$  is the strain-rate tensor.

Link between  $\mu$  and  $\lambda$  is

$$K = \frac{2}{3}\mu + \lambda \quad (2.11)$$

According to the Stokes' hypothesis, for incompressible and /or low Mach number flows:

$$K = 0.$$

Thus Eq. (2.11) will be:

$$\lambda = -\frac{2}{3}\mu \quad (2.12)$$

The strain-rate tensor,  $S_{ij}$ , will be:

$$S_{ij} = \frac{1}{2} \left( \frac{\partial u_i}{\partial x_j} + \frac{\partial u_j}{\partial x_i} \right) \quad (2.13)$$

Substituting Eq. 2.12 and Eq. 2.13 in Eq. 2.10, the viscous stress tensor will become:

$$\tau_{ij} = \mu \left[ \left( \frac{\partial u_i}{\partial x_j} + \frac{\partial u_j}{\partial x_i} \right) - \frac{2}{3} \left( \frac{\partial u_k}{\partial x_k} \right) \delta_{ij} \right] \quad (2.14)$$

For closing Navier-Stokes equations, we have to find the link between the thermodynamic variables  $(\rho, p, T, e, h)$ .

Using the perfect relations:

$$e = C_v T, \quad h = C_p T, \quad \gamma = \frac{C_p}{C_v}, \quad C_v = \frac{R}{\gamma-1}, \quad C_p = \frac{\gamma R}{\gamma-1} \quad (2.15)$$

So, the pressure will be:

$$p = (\gamma - 1)\rho e = (\gamma - 1)\rho \left( e_0 - \frac{1}{2} u_i u_i \right) \quad (2.16)$$

## 2.2 Reynolds Averaged Navier-Stokes (RANS) Equations

We derived RANS equations by decomposing flow variables into mean and fluctuating components as given below:

$$\phi = \bar{\phi} + \phi' \quad (2.17)$$

Here, the average of the viscous conservation laws is used for time  $T$  :

$$\bar{\phi} = \lim_{T \rightarrow \infty} \frac{1}{T} \int_t^{t+T} \phi(\mathbf{x}, t) dt \quad (2.18)$$

The time interval must be adequately large with respect to the time scales of the turbulent fluctuations; however, it should be small enough to suit all the other time-dependent factors. Here, the relations and correlation will be as follows:

$$\bar{\bar{\phi}} = \bar{\phi}, \quad \bar{\phi'} = 0, \quad \overline{\phi\psi} = \bar{\phi}\bar{\psi} + \overline{\phi'\psi'} \quad (2.19)$$

Eq.(2.1) becomes:

$$\frac{\partial}{\partial t} \int_V Q dV + \oint_S (F \cdot n) dS - \oint_S (F_v \cdot n) dS = \int_V S_T dV \quad (2.20)$$

Where:

$$Q = \left\{ \begin{array}{c} \bar{\rho} \\ \bar{\rho} \bar{u}_1 \\ \bar{\rho} \bar{u}_2 \\ \bar{\rho} \bar{u}_3 \\ \bar{\rho} \bar{e}_0 + (\bar{\rho}' e' + k) \end{array} \right\}, \quad F_j = \left\{ \begin{array}{c} \bar{\rho} \bar{u}_j + \bar{\rho}' \bar{u}'_j \\ \bar{\rho} \bar{u}_1 \bar{u}_j + \bar{p} \delta_{1j} + \bar{u}_1 \bar{\rho}' \bar{u}'_j + \bar{\rho}' \bar{u}'_1 \bar{u}_j \\ \bar{\rho} \bar{u}_2 \bar{u}_j + \bar{p} \delta_{2j} + \bar{u}_2 \bar{\rho}' \bar{u}'_j + \bar{\rho}' \bar{u}'_2 \bar{u}_j \\ \bar{\rho} \bar{u}_3 \bar{u}_j + \bar{p} \delta_{3j} + \bar{u}_3 \bar{\rho}' \bar{u}'_j + \bar{\rho}' \bar{u}'_3 \bar{u}_j \\ \bar{\rho} \bar{h}_0 \bar{u}_j + \bar{e}_0 \bar{\rho}' \bar{u}'_j + (\bar{\rho}' e' + k) \bar{u}_j \end{array} \right\} \quad (2.21)$$

$$F_{vj} = \left\{ \begin{array}{c} 0 \\ \bar{\tau}_{1j} - \tau_{1j}^T \\ \bar{\tau}_{2j} - \tau_{2j}^T \\ \bar{\tau}_{3j} - \tau_{3j}^T \\ \bar{u}_i \bar{\tau}_{ij} - \bar{q}_j + \Theta_j^T \end{array} \right\} \quad (2.22)$$

In this case, the kinetic energy is produced because of turbulent fluctuations ( $K$ ), and the Reynolds stress tensor  $\tau_{ij}^T$ . They are given below:

$$K = \frac{1}{2} \overline{\rho u'_i u'_i} \quad (2.23)$$

$$\tau_{ij}^T = \overline{\rho u'_i u'_j} \quad (2.24)$$

Here,  $\Theta_j^T$  has a turbulent heat flux tensor  $q_j^T$  while other turbulent terms are as follows:

$$\Theta_j^T = w_j^T - q_j^T - k_j^T - E_j^T \quad (2.25)$$

$$w_j^T = -\bar{u}_i \tau_{ij}^T + \bar{u}'_i \tau'_{ij} \quad (2.26)$$

$$q_j^T = \overline{\rho h' u'_j} \quad (2.27)$$

$$K_j^T = \frac{1}{2} \overline{\rho u'_i u'_i u'_j} \quad (2.28)$$

$$E_j^T = \bar{u}_i \overline{\rho u'_i u'_j} \quad (2.29)$$

For solving the above equations, all the turbulent terms should be modelled.

The weighted average of density:

$$\tilde{\phi} = \frac{\overline{\rho\phi}}{\bar{\rho}} \quad (2.30)$$

With the decomposition:

$$\phi = \tilde{\phi} + \phi'' \quad (2.31)$$

And the relations:

$$\overline{\tilde{\phi}} = \tilde{\phi} \quad \text{and} \quad \overline{\rho\phi''} = 0 \quad (2.32)$$

The Favre-averaged RANS equations will be:

$$\frac{\partial}{\partial t} \int_V Q dV + \oint_S (F \cdot n) dS - \oint_S (F_v \cdot n) dS = \int_V S_T dV \quad (2.33)$$

$$Q = \begin{Bmatrix} \bar{\rho} \\ \bar{\rho} \tilde{u}_1 \\ \bar{\rho} \tilde{u}_2 \\ \bar{\rho} \tilde{u}_3 \\ \bar{\rho} \tilde{e}_0 + k \end{Bmatrix} \quad F_j = \begin{Bmatrix} \bar{\rho} \tilde{u}_j \\ \bar{\rho} \tilde{u}_1 \tilde{u}_j + \bar{p} \delta_{1j} \\ \bar{\rho} \tilde{u}_2 \tilde{u}_j + \bar{p} \delta_{2j} \\ \bar{\rho} \tilde{u}_3 \tilde{u}_j + \bar{p} \delta_{3j} \\ \bar{\rho} \bar{h}_0 \tilde{u}_j + k \tilde{u}_j \end{Bmatrix} \quad (2.34)$$

$$F_{vj} = \begin{Bmatrix} 0 \\ \tilde{\tau}_{1j} - \tau_{1j}^T \\ \tilde{\tau}_{2j} - \tau_{2j}^T \\ \tilde{\tau}_{3j} - \tau_{3j}^T \\ \tilde{u}_i \tilde{\tau}_{ij} - \tilde{q}_j + \Theta_j^T \end{Bmatrix} \quad (2.35)$$

With,

$$K = \frac{1}{2} \overline{\rho u''_i u''_j} \quad (2.36)$$

$$\tau_{ij}^T = \overline{\rho u''_i u''_j} \quad (2.37)$$

$$\tilde{\tau}_{ij} = (\mu + \mu_t) \left[ \left( \frac{\partial \tilde{u}_i}{\partial x_j} + \frac{\partial \tilde{u}_j}{\partial x_i} \right) - \frac{2}{3} \left( \frac{\partial \tilde{u}_k}{\partial x_k} \right) \delta_{ij} \right] \quad (2.38)$$



$$q_i = -(K + K_t) \frac{\partial \tilde{T}}{\partial x_j} \quad (2.39)$$

$$\Theta_j^T = w_j^T - q_j^T - k_j^T \quad (2.40)$$

$$w_j^T = -\bar{u}_i \tau_{ij}^T + \overline{u_i'' \tau_{ij}''} \quad (2.41)$$

$$q_j^T = \overline{\rho h'' u_j''} \quad (2.42)$$

$$K_j^T = \frac{1}{2} \overline{\rho u_i'' u_i'' u_j''} \quad (2.43)$$

When the Reynold's average of the Navier-Stokes equations is taken, it adds several extra terms, which are modelled for closing the RANS equation system. Section 2.3 shows turbulence models, which were studied and their conditions were met. Comprehensive information pertaining to the Navier-Stokes as well as the RANS equations has been provided in the references [43 and 44].

### 2.3 Rotation and Velocity Triangle

For helicopter rotors, the far field shouldn't have rotation and only the flow near the helicopter rotor gets affected by the rotation. The velocity triangle is shown in Figure (2.1).

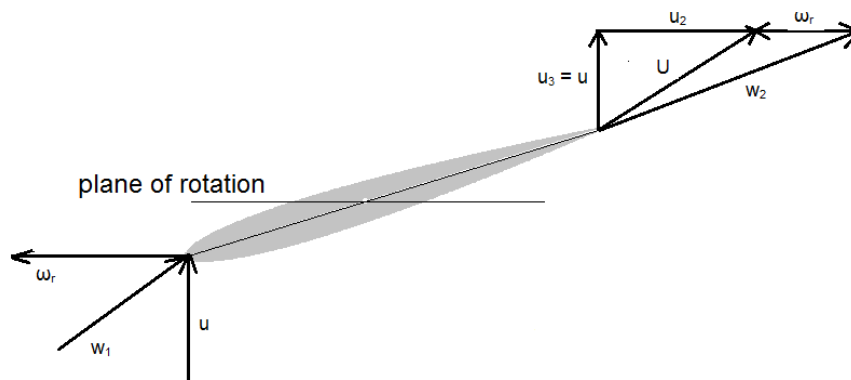


Figure 2. 1: Velocity triangle for a section of the rotor blade

Where:

$u$ : Axial velocity.

$U$ : Absolute velocity.

$u_2$ : Azimuthal component of the (absolute velocity).

$u_3$ : axial velocity component of the (absolute velocity).

$W_1$ : Relative velocity upstream of a blade.

$W_2$ : Relative velocity downstream of a blade.

## 2.4 Turbulence Models

Modelling turbulent terms in RANS equations is essential for solving them.

This study shows that three turbulence models are under investigation including the Spalart-Allmaras [45 , 46], Shear Stress Transport (SST) and the K- $\epsilon$  Launder–Sharma [47]. They  $\omega_r$ : Rotational velocity.

are based on RANS. They are also called as linear turbulent viscosity models.

### 2.4.1 Spalart-Allmaras Model

The Spalart-Allmaras model has a single equation but it is very popular because it is robust and facilitates complex flows. Its most significant advantage over the SST model is robustness. Other advantages include less CPU/memory use.

This model applies through resolving a single additional transport equation. This equation has one each of advective, diffusive and source term.

The turbulent viscosity is given by:

$$\nu_t = \tilde{\nu} f_{\nu 1} \quad (2.48)$$

Here,  $\tilde{\nu}$  is a turbulent variable while  $f_{\nu 1}$  is a function:

$$f_{\nu 1} = \frac{x^3}{x^3 + c_{\nu 1}^3} \quad (2.49)$$

In this case,  $x$  represents ratio between the working variable  $\tilde{\nu}$  and the molecular viscosity  $\nu$ .

$$x = \frac{\tilde{\nu}}{\nu} \quad (2.50)$$

The turbulent working variable follows the transport equation:

$$\begin{aligned} \frac{d\tilde{v}}{dt} = \frac{1}{\sigma} \{ \nabla \cdot [(\nu + \tilde{\nu}) \nabla \tilde{v}] + C_{b2} (\nabla \tilde{v})^2 \} + C_{b1} \tilde{S} \tilde{v} (1 - f_{t2}) \\ - \left\{ C_{w1} f_w - \frac{C_{b1}}{K^2} \right\} \left\{ \frac{\tilde{v}}{d} \right\}^2 + f_{t1} (\Delta q)^2 \end{aligned} \quad (2.51)$$

Where:

$\tilde{v}$  represents working variable and  $\nu$  represents molecular viscosity.

The constants and functions given in equations (2.43) to (2.45) are presented below:

$$\tilde{S} = S + \frac{\tilde{v}}{k^2 d^2} f_{v2}, \quad f_{v2} = 1 - \frac{x}{1 + x f_{v1}} \quad (2.52)$$

Here  $d$  represents distance to the wall,  $k$  represents Von Karman constant while  $S$  shows the magnitude of the vorticity.

The function  $f_w$  is given below:

$$f_w = g \left( \frac{1 + C_{w3}^6}{g^6 + C_{w3}^6} \right)^{1/6} \quad (2.53)$$

Where:

$$g = r + C_{w2} (r^6 - r) \quad \text{and} \quad r = \frac{\tilde{v}}{\tilde{S} k^2 d^2} \quad (2.54)$$

The functions  $f_{i1}$  and  $f_{i2}$  are given by:

$$f_{i1} = c_{i1} g_i \exp \left[ -c_{i2} \left( \frac{w_i}{\Delta q} \right)^2 (d^2 + g_i^2 d_i^2) \right], \quad f_{i2} = c_{i3} \exp(-c_{i4} X^4) \quad (2.55)$$

Where:

$w_i$  : The wall vortices at the trip.

$d_i$  : The field point-trip distance

$\Delta q$  : The velocity difference between the trip and the field point.

$g_i; g_i = \min [1.0, \Delta q / w_i \Delta x]$ , with  $\Delta x$  being the grid spacing along the wall at the trip.

The constants used so far are:

$$\sigma = \frac{2}{3} , \quad c_{b1} = 0.1355 , \quad c_{b2} = 0.1355 , \quad k = 0.41 ,$$

$$c_{w1} = \frac{c_{b1}}{k^2} + (1 + c_{b1})/b = 2.5093$$

$$c_{w2} = 0.3 , \quad c_{w3} = 2.0 , \quad c_{v1} = 7.1 , \quad c_{t1} = 1.0 , \quad c_{t2} = 2.0 , \quad c_{t3} = 1.1 , \quad c_{t4} = 2.0$$

### 2.4.2 $k - \varepsilon$ Model

In this model, Launder-Sharma and low Reynold's Number are utilized. The low Reynolds number model has advantage over a standard model that a standard model uses numerically unstable values when the integration with the wall takes place. On the other hand, the low Reynolds number  $k - \varepsilon$  facilitates direct integration of the viscous sub layer to the wall [48]. This low Reynolds number model has been expressed using turbulent kinetic energy and turbulent dissipation rate equations, which are given below:

$$\rho \frac{DK}{Dt} = \frac{\partial}{\partial x_j} \left[ \left( \mu + \frac{\mu_t}{\sigma_k} \right) \frac{\partial k_j}{\partial x_j} \right] + P_k - \rho \varepsilon + L_k \quad (2.56)$$

And

$$\rho \frac{D\varepsilon}{Dt} = \frac{\partial}{\partial x_j} \left[ \left( \mu + \frac{\mu_t}{\sigma_\varepsilon} \right) \frac{\partial \varepsilon}{\partial x_j} \right] + c_{\varepsilon 1} f_1 P_k \frac{\varepsilon}{K} - c_{\varepsilon 2} f_2 \rho \frac{\varepsilon^2}{k} + L_\varepsilon \quad (2.57)$$

Where:  $P_k$  is the turbulent production defined as.

$$P_k = \tau_{ij} \frac{\partial u_i}{\partial x_j} \quad (2.58)$$

The turbulent viscosity  $\mu_t$  is computed as:

$$\mu_t = \rho f_\mu c_\mu \frac{K^2}{\varepsilon} \quad (2.59)$$

The coefficients of the  $k - \varepsilon$  model are presented in Table (2.1):

Table 2. 1: Coefficients of the K- $\varepsilon$  models

$K - \varepsilon$ model	Launder-Sharma
$c_\mu$	0.09
$c_{\varepsilon 1}$	1.44
$c_{\varepsilon 2}$	1.92
$\sigma_k$	1.0
$\sigma_\varepsilon$	1.3
$f_\mu$	$e^{\left[\frac{-3.4}{(1+Re_t/50)^2}\right]}$
$f_1$	1.0
$f_2$	$1 - 0.3e^{-Re_t^2}$ $Re_t = \frac{k^2}{\nu\varepsilon}$
$L_k$	$-2\mu \left(\frac{\partial\sqrt{k}}{\partial x_j}\right)^2$
$L_\varepsilon$	$-2\mu \frac{\mu\mu_t}{\rho} \left(\frac{\partial^2 u_i}{\partial x_j^2}\right)^2$

### 2.4.3 Mode $k - \omega$ Shear Stress Transport (SST)

The  $k - \omega$  turbulence model consists of a two-equation model. The first equation expresses the kinetic turbulent energy  $k$  and the second shows specific turbulent dissipation rate  $\omega$ . Just like  $k - \varepsilon$ ,  $k - \omega$  model has been presented in several versions.

The SST model's transport equations are given below:

$$\rho \frac{dk}{dt} = \frac{\partial}{\partial x_j} \left[ (\mu + \sigma_k \mu_t) \frac{\partial k}{\partial x_j} \right] + P_k - \beta^* \rho \omega k \quad (2.60)$$

$$\rho \frac{d\omega}{dt} = \frac{\partial}{\partial x_j} \left[ (\mu + \sigma_\omega \mu_t) \frac{\partial \omega}{\partial x_j} \right] + \gamma P_k \frac{\omega}{k} - \beta \rho \omega^2 + 2(1 - F_1) \rho \sigma_{\omega 2} \frac{1}{\omega} \frac{\partial k}{\partial x_j} \frac{\partial \omega}{\partial x_j} \quad (2.61)$$

Here, the constant  $\beta^* = 0.09$ . The last right-side term in the Eq. (2.61) represents cross diffusion, which is only activated outside the boundary layer. Moreover,  $F_1$  represents blending function, which blends the coefficients of the genuine  $k - \omega$  model within the boundary-layer zone.

Equations (2.60) and (2.61) have constants, which are expressed below in the compact form:

$$\phi = F_1 \phi_1 - (1 - F_1) \phi_2 \quad (2.62)$$

Where:

$\phi_1$  Constants of the  $k - \omega$  model (when  $F_1 = 1$ )

And

$\phi_2$  Constants of the  $k - \varepsilon$  model (when  $F_1 = 0$ )

Now,  $\beta, \gamma, \sigma_\omega$  and  $\sigma_k$  are defined in terms of blending coefficients:

- Inner model constants  $\beta_1 = 0.075, \gamma_1 = 0.5532, \sigma_{\omega_1} = 0.5, \sigma_{k_1} = 0.5$
- Outer model constants  $\beta_2 = 0.082, \gamma_2 = 0.4403, \sigma_{\omega_2} = 0.856, \sigma_{k_2} = 1.0$

The blending function  $F_1$  is defined by:

$$F_1 = \tanh \left\{ \min \left[ \max \left( \left( \frac{\sqrt{k}}{\beta^* \omega d}, \frac{500\nu}{\omega d^2} \right), \frac{4\rho\sigma_{\omega 2}k}{CD_{k\omega}d^2} \right) \right] \right\} \quad (2.63)$$

Where:

$$CD_{\omega k} = \max \left( 2\rho\sigma_{\omega 2} \frac{1}{\omega} \frac{\partial k}{\partial x_j} \frac{\partial \omega}{\partial x_j}, 1.0e^{-20} \right) \quad (2.64)$$

Note,  $d$  being the distance to the nearest surface.

## 2.5 Boundary Conditions

The boundary conditions have two types, which can be simulated through the CFD simulation of a helicopter rotor blade. They can be classified as solid wall and external (or farfield) boundary conditions.

### 2.5.1 Solid Wall Boundary Conditions

The boundary conditions of the turbulent wall are handled using the following models:

a) Spalart-Allmaras **Model:**

This turbulence model assumes the turbulent working variable as fixed at zero:

$$\tilde{\nu} = 0 \quad (2.65)$$

b)  $k - \omega$  **Model:**

For the  $k - \omega$  model, the boundary condition on the solid wall is as follow:

$$\omega_{wall} = \frac{60\nu}{\beta_1 d^2} \quad (2.66)$$

$$k_{wall} = 0 \quad (2.67)$$

### 2.5.2 External Boundary Conditions, (Farfield B.C)

The farfield boundary conditions need application of the Riemann invariants or the non-reflective boundary conditions. Their details have been provided in the references section [49, 50, 66].

These boundary conditions are uniform at the farfield because at that position, their velocities remain unaffected by the blade rotation. The blocks, which are closer to the blades, their flow is influenced by the rotational movement. The code handles interaction between the stationary and rotating blocks.

The temperature, static pressure, and axial velocity define the external boundary conditions, which are obtained through the experimental data while the turbulent kinetic energy  $\mathcal{K}$  the turbulent viscosity  $\nu_t$  and the turbulent dissipation rate  $\epsilon$  can be computed as follows:

The computation of the dynamic viscosity can be done using Sutherland's law [51]:

$$\mu = \mu_{ref} \left( \frac{T}{T_{ref}} \right)^{3/2} \frac{T_{ref} + S}{T + S} \quad (2.68)$$

Where:

$\mu_{ref}$  : Viscosity at  $T_{ref}$

$T_{ref}$  : Reference temperature

$S$  : Sutherland temperature

Since air is treated as perfect gas in this study, the calculated coefficients according to Sutherland's law are given in Table (2.2):

Table 2. 2: Sutherland's law Coefficient

Gas	$\mu_{ref}$ (kg/ms)	$T_{ref}$ (K)	$S$ (k)
Air	$1.716 \times 10^{-5}$	273.15	120

Using Eq. (2.69), the kinematic viscosity was computed:

$$v = \mu / \rho \quad (2.69)$$

Consequently, the turbulent viscosity is computed for external flows [52].

$$\nu_{T \text{ external}} = \nu_{\text{external}} \quad (2.70)$$

The turbulent kinetic energy is computed using the turbulent intensity by the following formula:

$$T_u = \frac{\sqrt{\hat{u}^2}}{U_{ref}} \quad (2.71)$$

In case of external flow, the turbulent intensity is decreased to 1% [43], so:

$$K = \frac{3}{2} \left( \sqrt{\hat{u}^2} \right)^2 \quad (2.72)$$

Using the turbulent dissipation value,  $\varepsilon$  can be computed using the formula given below:



$$\varepsilon = C_{\mu} \frac{\mu}{\mu_t} \frac{\rho_{ref} K^2}{\mu} \quad (2.73)$$

Here  $C_{\mu} = 0.09$  .

## 2.6 Figure OF Merit (FM)

The Figure of Merit is a concept that is very popular for measuring the rotor's hovering efficiency, which is actually the ratio between the least possible power requirement for hovering and the actual power needed for hovering. Further information on Figure of Merit (FM) has been provided in the references section [53].

In the nutshell, the Figure of Merit helps comparing the actual rotor performance with the ideal rotor performance.

$$FM = \frac{\text{Ideal Induced Power}}{\text{Actual Power}}$$

Hence the figure of merit is given by:

$$FM = \frac{ct^{3/2}}{\sqrt{2} \cdot cp} \quad (2.75)$$

Consequently, Equation 2.75 shows FM value for a given rotor that increases when the CT increases. It means that the researchers should be careful while using the FM to compare. Generally, 0.75 is a good value for Figure of Merit while the profile-drag accounts for approximately ¼ of the overall rotor power.

## **CHAPTER 3**

### **VALIDATION STUDY**

This chapter discusses the outcomes of the simulations of 3-D steady state Computational Fluid Dynamics (CFD) by presenting two test cases. The first case is Caradonna-Tung, which was used in the testing facility of the Army Aero-mechanics Lab for conducting hovering tests. At the facility area, there was a large wind tunnel that was specifically designed with ducts to eliminate the re-circulation of air. The second case was the UH-60A Black Hawk helicopter rotor, which was used for testing in the hovering conditions. Both the test cases were considered for validating the commercial NUMECA CFD software. Moreover, three other turbulence models were tested and the results were compared with the experimental data. Choosing the best available turbulence model is essential for finding the most accurate solution that will be further utilized during the remaining part of this thesis.

#### **3.1 Test Case I: Caradonna –Tung Helicopter Rotor Blade**

##### **3.1.1 Experimental Data and Blade Description**

In the first case, Caradonna-Tung (1981) [31] was used to carry out an experimental study, during which, the model helicopter rotor was operated and analyzed during the hovering condition. The Army Aeromechanics Lab maintained the database, which was collected during the hovering test. Later, many European research labs contributed to this database, and the laboratory documented it for offering the results to the researchers.

In the studied case, the rotor used a couple of cantilever-mounted blades with manual adjustment options. Those blades had NACA 0012 profile with untwisted as well as untapered shape as shown in Figure 3.1. The aspect ratio  $AR = 6$ , the model rotor diameter was 2.286m (7.5 feet), and the length of fixed chord along the span was 0.1905m (0.625 feet) as Figure 3.2 shows.

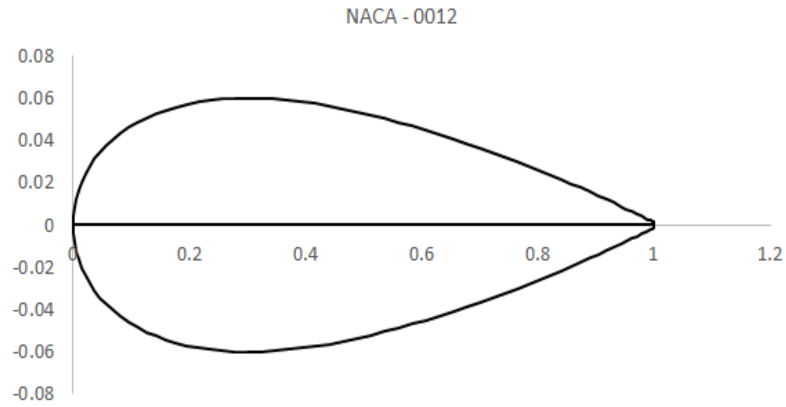


Figure 3. 1: NACA 0012 Airfoil Geometry

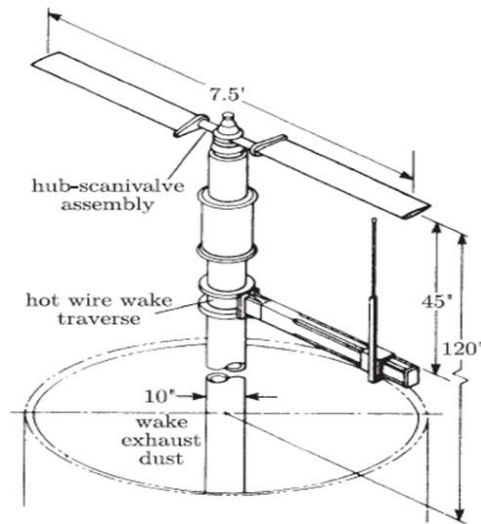


Figure 3. 2: Caradonna-Tung two-blade model rotor while hovering [31]

No details are available about the tip shape or the hub geometry in this experiment. Piotr and Oskar [28] have used Caradonna – Tung for computing flat-tip surfaces as well as sharp trailing edges of all the blades. Artificial-hub cylindrical surface with radius  $R_{ahub} = 0.5c$  replaced the shaft's real shape as Figure 3.3 shows. The inner rotor radius was assumed as  $R_{in} = c$ .

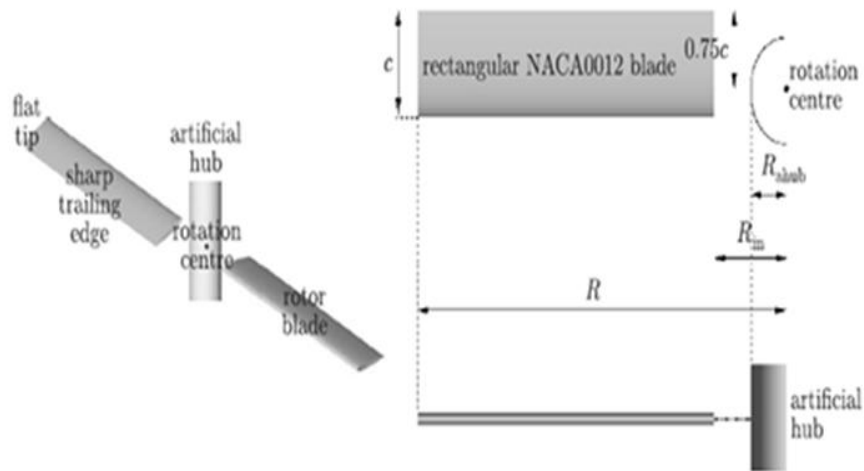


Figure 3. 3: Geometry of Caradonna-Tung rotor, [28]

Table 3. 1: The real blade of Caradonna-Tung

Airfoil section	NACA 0012
Number Of Blades	2 rectangular
Collective Pitch Angle	8 degrees
Rotor Diameter	2.286 m
Blade Chord Length	0.1905 m
Aspect Ratio	AR 6
Rotation speed RPM	1250-1750-2500 rpm
Ambient Pressure $P_{atm}$	103 027 Pa
Ambient Temperature $T_{atm}$	289.75 K
Ambient Density $\rho_{atm}$	1.2389 [Kg/M <sup>3</sup> ]
Untwisted & Untapered	0 degrees along the span

Experiments were repeated with many rotation rates and collective pitch settings. Collective pitch angles of 5° and 8° with tip Mach numbers 0.439, 0.612, 0.794 and 0.877 at rotor speeds 1250, 1750 and 2500 rpm were tested.

In order to assure the computational efficiency, just one blade was used with the rotor. During the Caradonna-Tung experiments, the surface pressure distribution was calculated in 5 span-wise sections:  $r/R = 50\%$ ,  $68\%$ ,  $80\%$ ,  $89\%$  and  $96\%$ .

### 3.1.2 Aerodynamic pressure coefficient

Using Eq. 3.1, the pressure coefficient can be calculated as:

$$C_p = \frac{P - P_\infty}{0.5 \rho_\infty (U_\infty^2 + (\Omega r)^2)} \quad (3.1)$$

Where:

- $U_\infty$  : The wind speed [m/sec]
- $\rho_\infty$  : The free stream density [Kg/m<sup>3</sup>]
- $r$  : Radial distance between the hub center and the blade section [m]
- $\Omega$  : The rotational speed [rad/sec]

During hovering condition  $U_\infty$ , the wind speed remained zero; therefore, the equation of pressure coefficient can be expressed as:

$$C_p = \frac{P - P_\infty}{0.5 \rho_\infty (\Omega r)^2} \quad (3.2)$$

## 3.2 Simulation and Results for Caradonna-Tung Blade

### 3.2.1 Geometric Blade

The geometric blade of Caradonna-Tung was generated using the AutoBlade [55] software of NUMECA. The geometric blade is shown in figures 3.4 and 3.5.

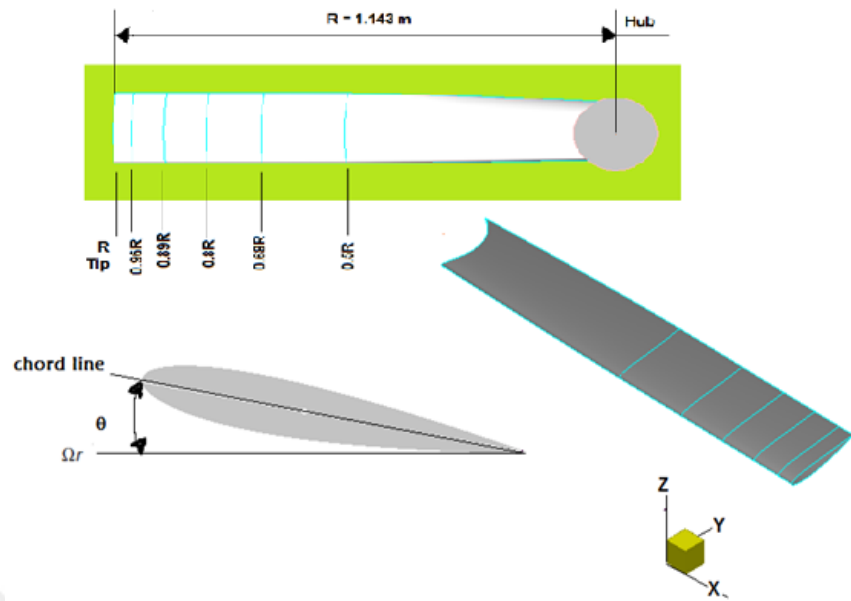


Figure 3. 4:3D Caradonna-Tung blade geometry generated by AutoBlade

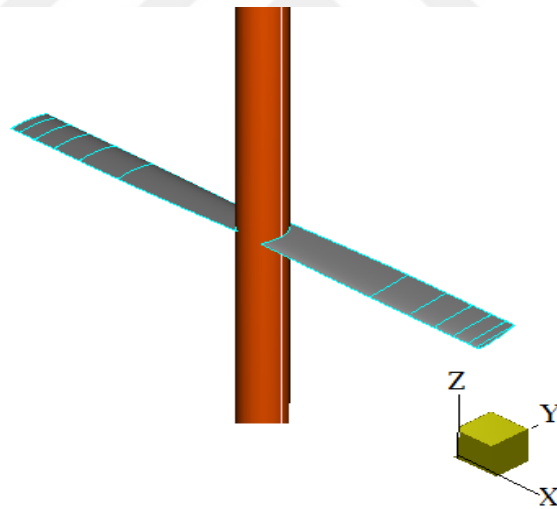


Figure 3. 5:3D view

### 3.2.2 Mesh Generation

The calculations in this study were performed with the help of CFD package called as FINE/Turbo solver [56], which was developed by NUMECA International. That FINE/Turbo solver offers 3D structured, density-based, multi-blocked finite volume code. In this case, mesh generation is performed through O4H grid topology.

The IGG/AutoGrid-5 software was used for generating grid [57], which was developed by Numeca International. The 5-block mesh schematic diagram is presented below as Figure 3.6 shows.

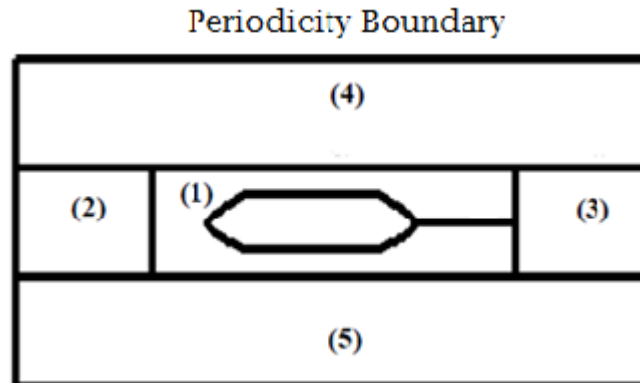


Figure 3. 6:(O4H ) grid block structure used

1. The block around-the-blade O-block is called as the skin block.
2. The H-block above the blade's leading edge is called as the inlet block.
3. The H-block below the trailing edge is termed as the outlet block.
4. The H-block on the blade section is called as the up block.
5. The H-block closer to the blade section is called as the down block.

The hovering rotor's mesh was generated for single blade while the periodic conditions were applied to account for the other blade. This decreases the simulation time. The first cell's width was found using the Blasius Equation.

### 3.2.3 Estimate the width of the first cell at the wall

The first cell width should be selected carefully because the flow solution quality generally depends on capturing the flow phenomena taking place within the boundary layers that develops along the solid walls.

Depending on the selected turbulence model, NUMECA recommends finding the closest grid point along the wall having a distance corresponding with the parietal coordinate  $y^+$  that ranges between 1 and 5 (Low Reynold's number model).

The Blasius Equation helps finding the link between the first cell's width and the parietal coordinate  $y^+$ . Here, Blasius Equation drives  $y^+$  [57], which is expressed for turbulent flows as given below:

$$Y_{\text{wall}} = 6 \left( \frac{V_{\text{ref}}}{\nu} \right)^{-\frac{7}{8}} \left( \frac{L_{\text{ref}}}{2} \right)^{\frac{1}{8}} Y_1^+ \quad (3.1)$$

Here:

- $Y_{\text{wall}}$  represents the distance between the nearest grid point and the wall (in meters).
- $V_{\text{ref}}$  represents the flow's reference velocity or the inlet velocity (m/s).
- $\nu$  shows the fluid's kinematic viscosity ( $\text{m}^2/\text{s}$ ) that is obtained by dividing the dynamic viscosity by the density.
- $L_{\text{ref}}$  shows the test case's reference length (in meters) while  $Y_1^+$  is a dimensionless value.

In the present case, we can estimate that  $V_{\text{ref}} = 299 \text{ m/s}$ ;  $L_{\text{ref}} = 0.1905 \text{ m}$ ,  $\nu = 1.7\text{e-}5 \text{ m}^2/\text{s}$ . Assuming that if we want to get  $Y^+$  around 1 at the wall, it turns out that  $Y_{\text{wall}} = 2.11 \times 10^{-6} \text{ m}$ .

The hovering simulation in this case study is carried out on coarse, fine, and finer 3D meshes. The CFD mesh pertaining to high and low resolution below as well as closer to the rotor tip was initiated for finding its impact on the tip-vortex visualization. Using Navier-Stokes calculations, the coarse mesh sizes were found adequate for predicting blade loading; however, in order to carry out correct predictions of wake and trajectory, there is a need for fine mesh resolution because it decreases diffusion and dispersion issues taking place in the coarse mesh. The computational body-fitted structured grid is semi-automatically generated with the help of parameterised python scripts of the IGG/AutoGrid5 software.

### 3.2.4 Mesh Study and Validation Results

The Numeca AutoGrid mesh generator was used for generating the mesh, and it was generated for a single blade under periodic conditions, which are similar to the conditions as if the other blade has been used. The study was conducted in this case at



high rotation speed (2500 rpm) from coarse to fine and then finer meshes with resolutions of 131427, 965334 and 7391004 nodes respectively.

Table 3.2 summarizes the different grid levels used in the mesh study and the time taken for one convergent solution.

Table 3. 2: Different grid system for Caradonna-Tung rotor at 2500 rpm

Mesh name at hover	Number of Grid 3D mesh	FM	Time work
Coarse	131427	0.420	1 hr
Fine	965334	0.538	3 hr
Finer	7391004	0.553	12 hr

The properties of the computer used :

Intel (R) Core (TM) i5 – 3210M CPU @ 2.50 GHz 2.50 GHz / RAM 8GB / 64BT/ name VAIO.

In Figure 3.7, a cut through the grid at  $r/R=0.5$  has been projected on  $z$  has been presented showing orthogonal shape and smoothness of the 2D mesh.

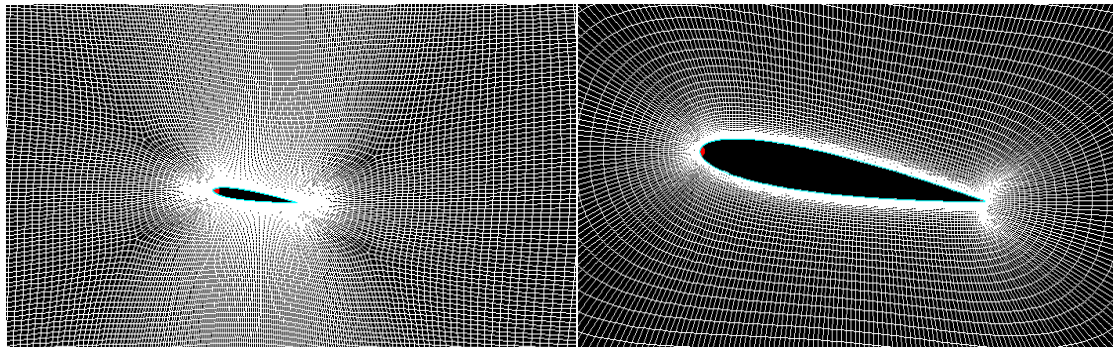


Figure 3. 7:2D mesh at blade mid-span of Caradonna-Tung rotor

The computational domain, which stands for the blade mesh, and the external field of Caradonna-Tung rotor, showed the total number of the block structures, which are illustrated in Figure3.8.

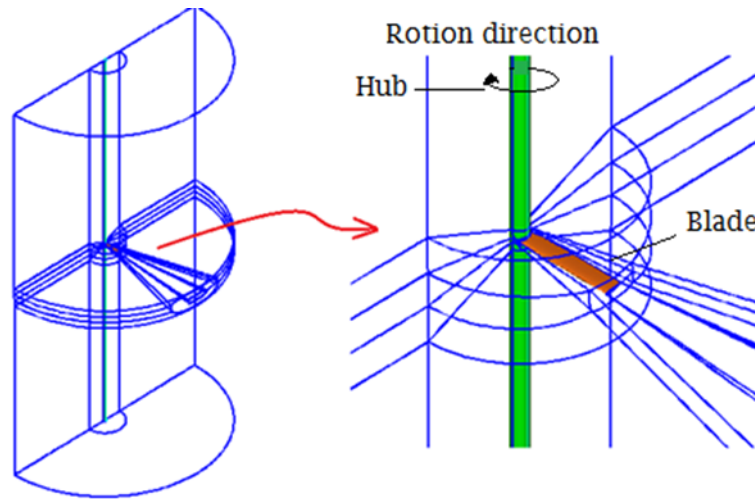


Figure 3. 8:3D Mesh block structure for Caradonna-Tung rotor

The hovering rotor flow simulations were calculated and the calculations were performed assuming that the wake shed is periodic with respect to time and space, and the flow closer to the hovering rotor is considered as a steady-state problem.

The Fine/Turbo solver is used to solve the 3D steady-state RANS equations with three turbulence models [56]. Those turbulence models include Spalart-Allmaras, Shear Stress Transport (SST), and the  $K - \epsilon$  Launder-Sharma Model, which were applied with the help of local time stepping for every cell.

The validation case is the experimental data for the total pitch angle of 8 degrees at the rotational speed of 2500rpm.

The Figure 3.9 shows the comparison between the experimental pressure coefficient distribution and the computed CFD pressure coefficient distribution solved using Spalart-Allmaras at different mesh values for Caradonna-Tung rotor at three span-wise sections; 50%, 80%, and 96% with maximum 4000 iterations.

By looking at the previous results, it was found that the fine mesh passes through the experimental solution points more conveniently as compared to the other forms. From this observation, it was concluded that the fine grid or mesh is closer to the experimental solution, and it also serves as a solution to other problems pertaining to the rotation speed.

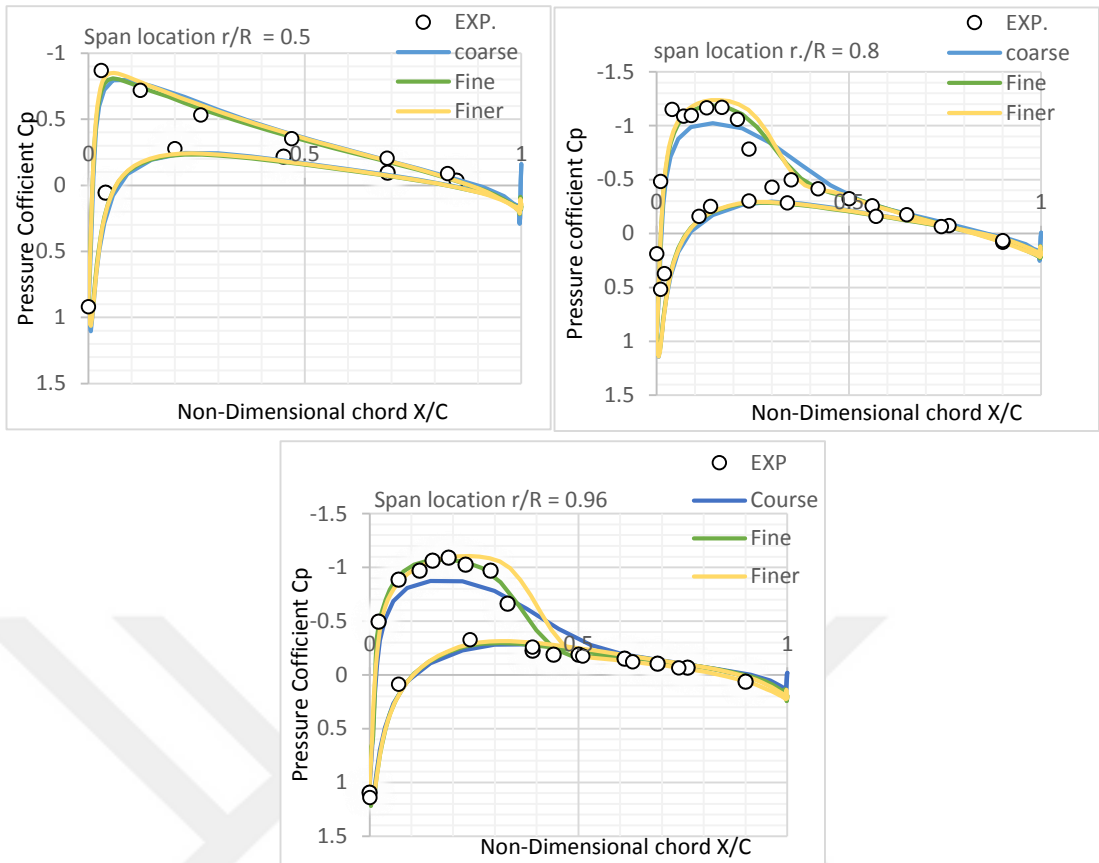


Figure 3. 9: Pressure coefficient distribution comparison between experimental and CFD calculated at 50%, 80%, 96% span-wise at different mesh levels.

The  $Y^+$  value located between 1 and 3 in the wall blade. Such range of is suitable for the tested Spalart-Allmaras turbulence model, the figure 3.10 is show that.

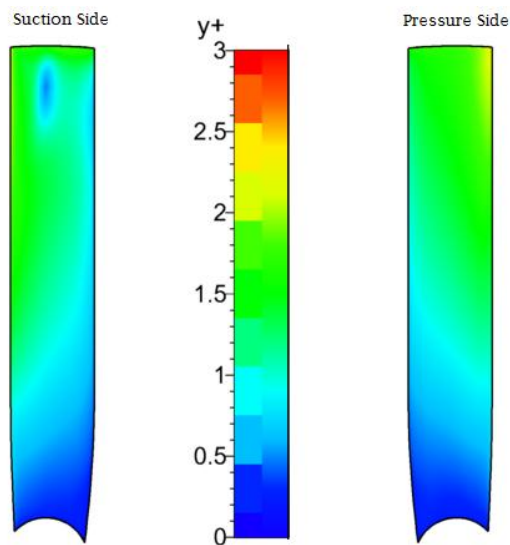


Figure 3. 10:  $Y^+$  Value for Caradonna - Tung at 2500 rpm

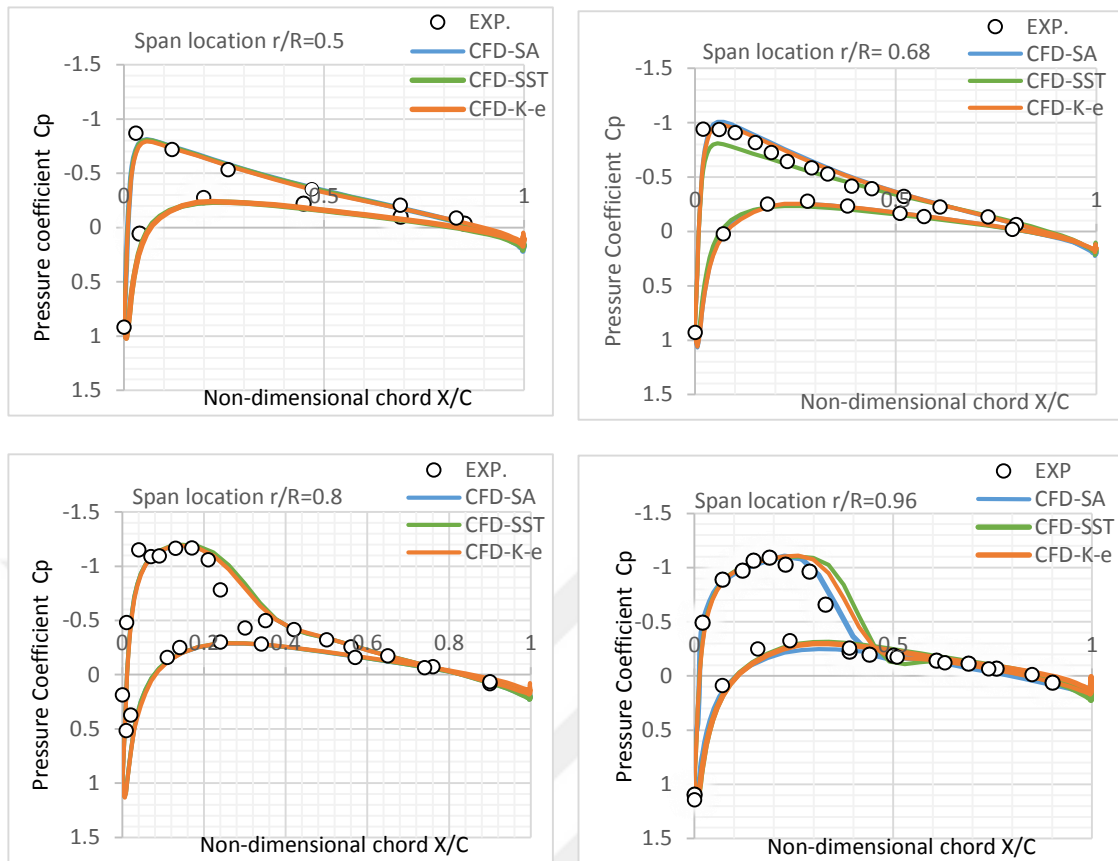


Figure 3. 11:Pressure coefficient distribution comparison between experimental and CFD using different turbulence models

Figure 3.11 illustrates the distribution of pressure coefficients in several turbulence model solutions such as Spalart-Allmaras, the  $K - \epsilon$  model and the Shear Stress Transport (SST) model with the experimental data for Caradonna-Tung [ 31] rotor craft at spanwise locations of  $r/R= 0.5, 0.68, 0.8,$  and  $0.96$

The 3-D gauge pressure contours on both pressure and suction sides of the blade are shown in Figure 3.12 using the Spalart-Allmalas turbulence model at rotation speed:  $\Omega = 2500$  rpm.

The static stream pressure difference is equal to the gauge pressure, which can be mathematically expressed as:

$$P_{static} - P_{\infty} = P_{gauge}$$

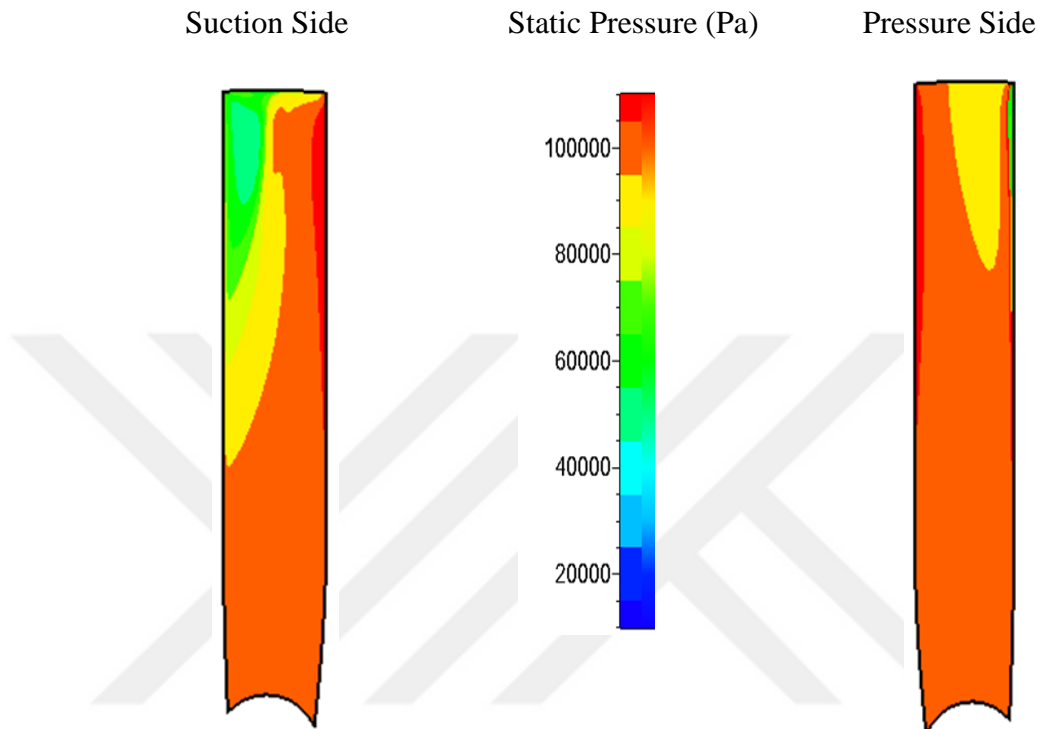


Figure 3. 12;Gauge pressure contours for Caradonna - Tung at 2500 rpm

Figure 3.12 shows considerable pressure variation in both the span-wise and chord-wise directions at 2500rpm. This variation becomes higher closer to the blade tip.

Figures 3.13 to 3.16 show the gauge pressure contours' results both on pressure and suction sides of the blade at 1250 RPM and 1750 RPM respectively.

Computed coefficient of pressure distributions at five span-wise blade sections of  $r/R = 0.5, 0.68, 0.80, 0.89$  and  $0.96$  at different rotation speeds: 1250rpm and 1750rpm.

The results at 0.5, 0.80 and 0.96 span-wise are shown in Figures 3.13 and 3.16 below.

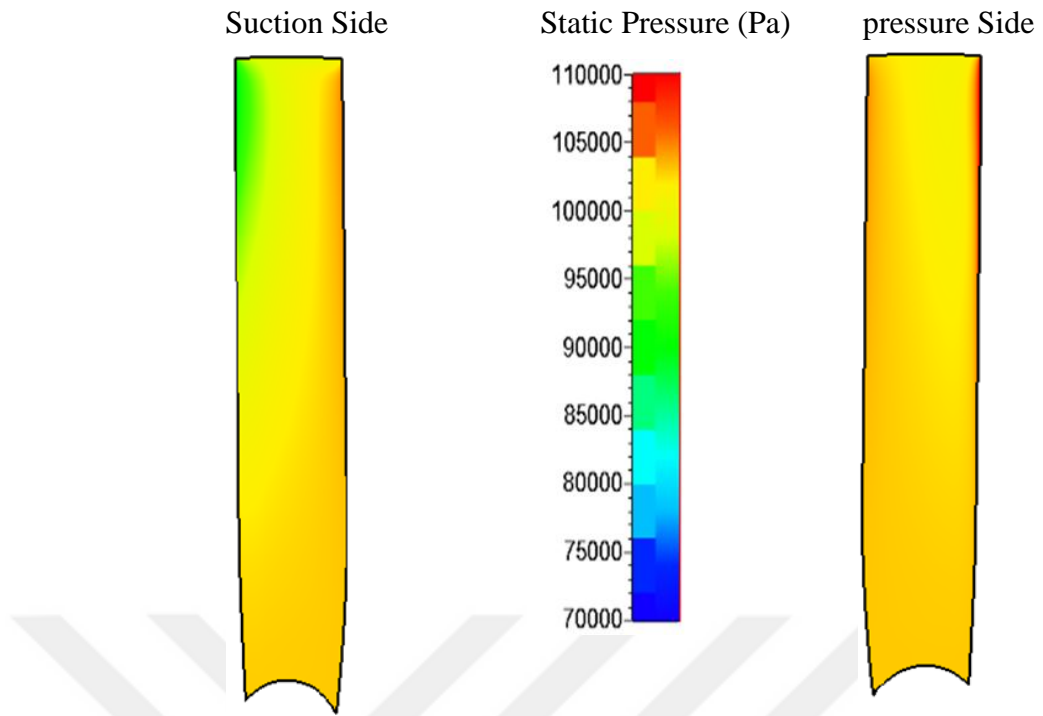


Figure 3. 13:Gauge pressure contours for Caradonna - Tung at 1250 rpm

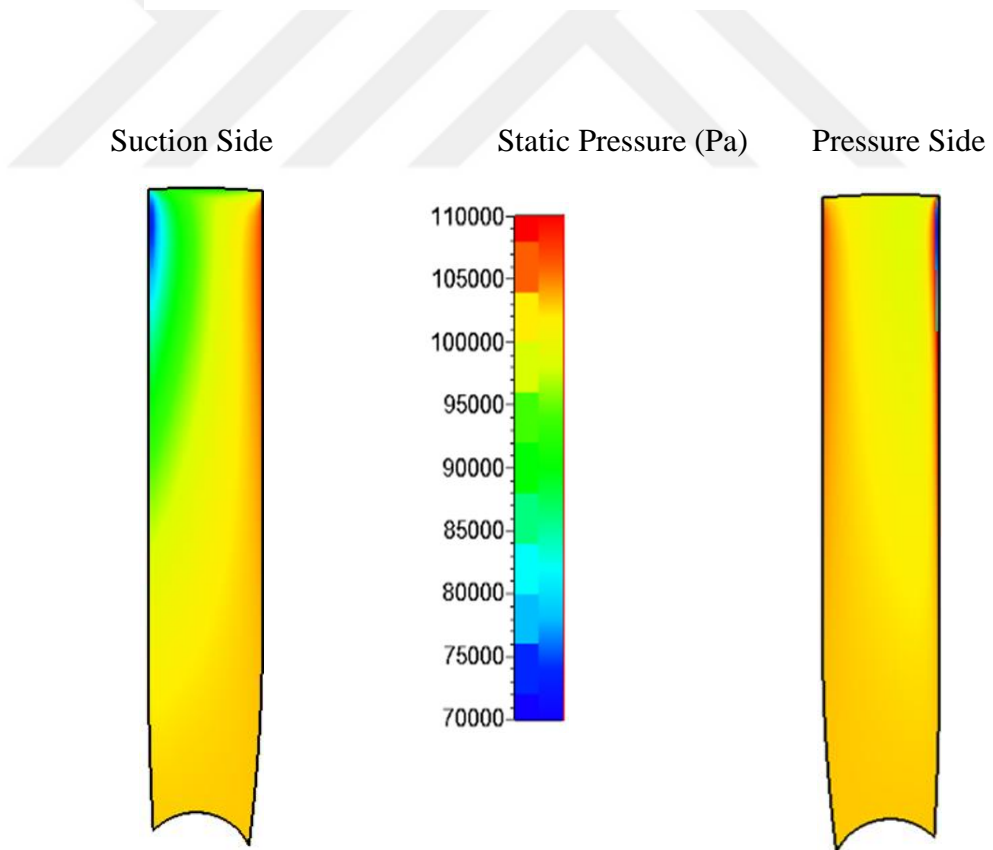


Figure 3. 14:Gauge pressure contours for Caradonna -Tung at 1750 rpm

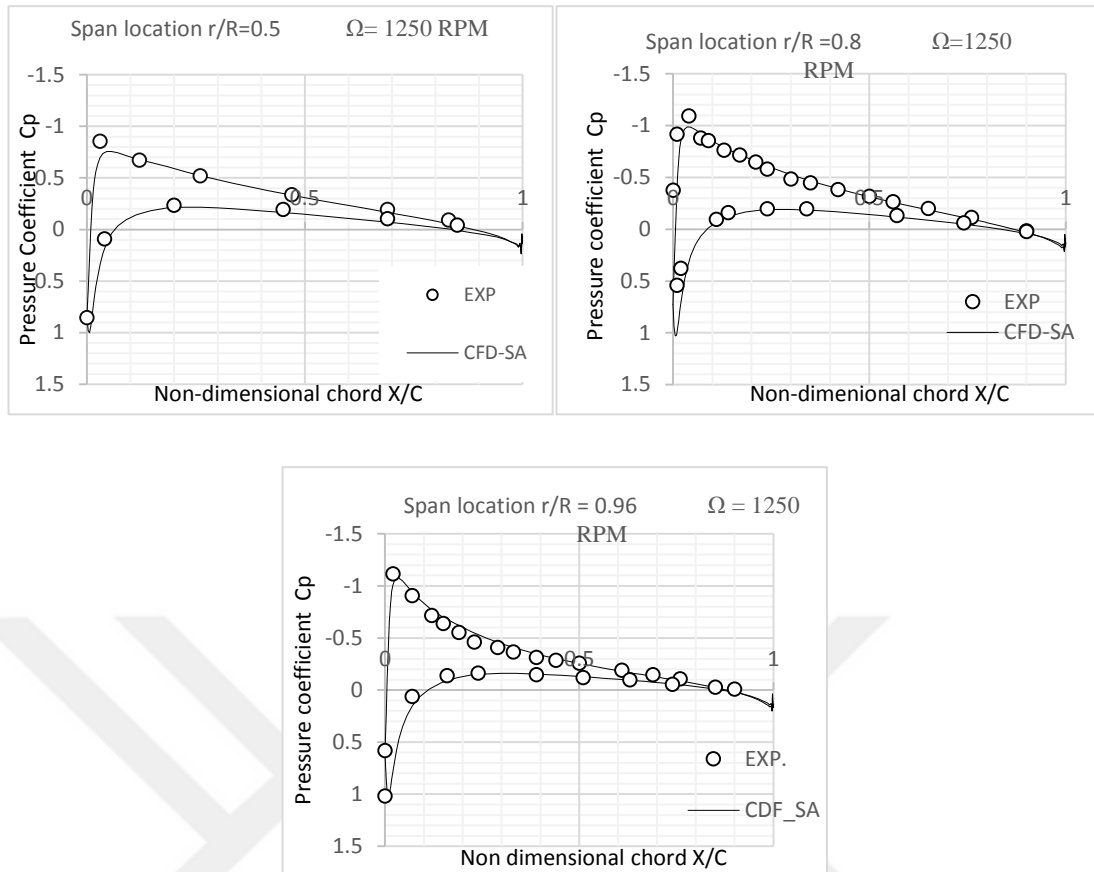


Figure 3. 15: Comparison between Numerical (SA) and experimental at different span-wise sections at 1250 rpm

At 1250 and 1750 rpm, the CFD pressure coefficient distribution at every section along the blade span shows good agreement with the experimental data. These rotational speeds allow the flow to be fully attached to the blade without any separation.

At high rotation speed 2500 rpm, a great discrepancy emerged between the experimental and computed pressure distributions on the pressure side with inboard spans 68%, 80% and 96%. At these points, the rotational speed separation has occurred, which strengthened the formed vorticity that is stronger near the root as shown in Figure 3.11.

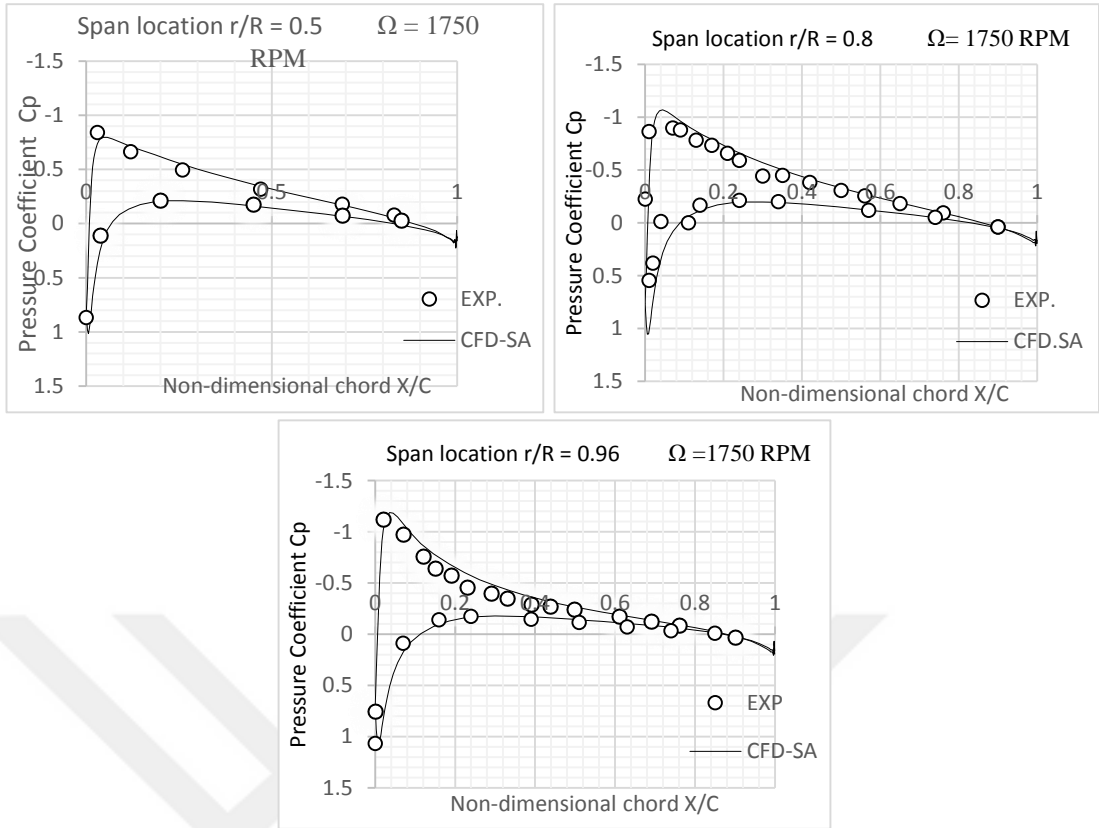


Figure 3. 16: Comparison between Numerical (SA) and experimental at different span-wise sections at 1750 rpm

The figure below shows the results of the experimental data and CFD computations for thrust force and the thrust coefficients at each rotation speed  $\Omega = 1250, 1750, 2250,$  and  $2500$  rpm with different turbulence models.

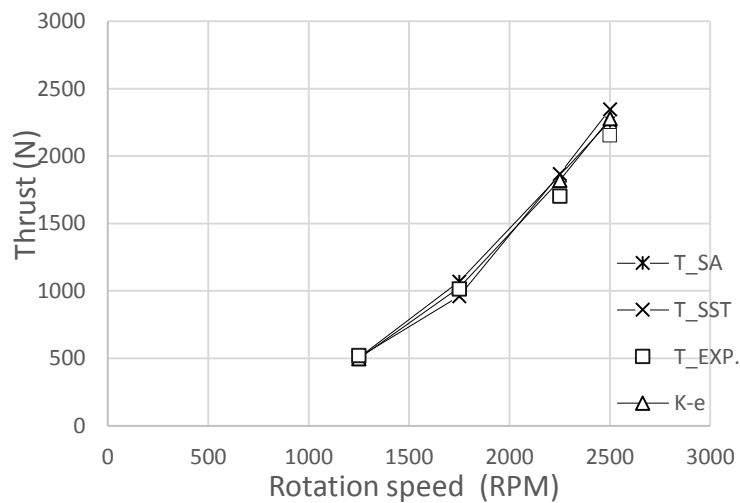


Figure 3. 17: Comparison of experimental Thrust with different turbulence models Thrust for Caradonna -Tung



Figure 3.17 shows that all the considered models exhibited reasonable agreement with the experimental data; however, it was noted that the results obtained through Spalart-Allmaras were the closest to the experimental data as compared to the other two turbulence models; therefore, we excluded them from further discussion. All the models showed similar behaviours regarding the prediction of thrust at different rotational speeds.

The calculated span-wise distributions pertaining to the lift coefficient at  $\Omega= 1250\text{rpm}$ ,  $1750\text{rpm}$  and  $\Omega= 2500\text{rpm}$  were compared to the experimental data as the Figure 3.18 shows.

The experimental results are plotted in two different ways; one way is directly obtained from the lift coefficient data of Caradonna–Tung experiment report, and the second is obtained by integrating the pressure coefficients of the experiment conducted along the chord in the corresponding section [32].

The computational results for sectional lift coefficient at three rotation speeds showed agreement with the experimental data.

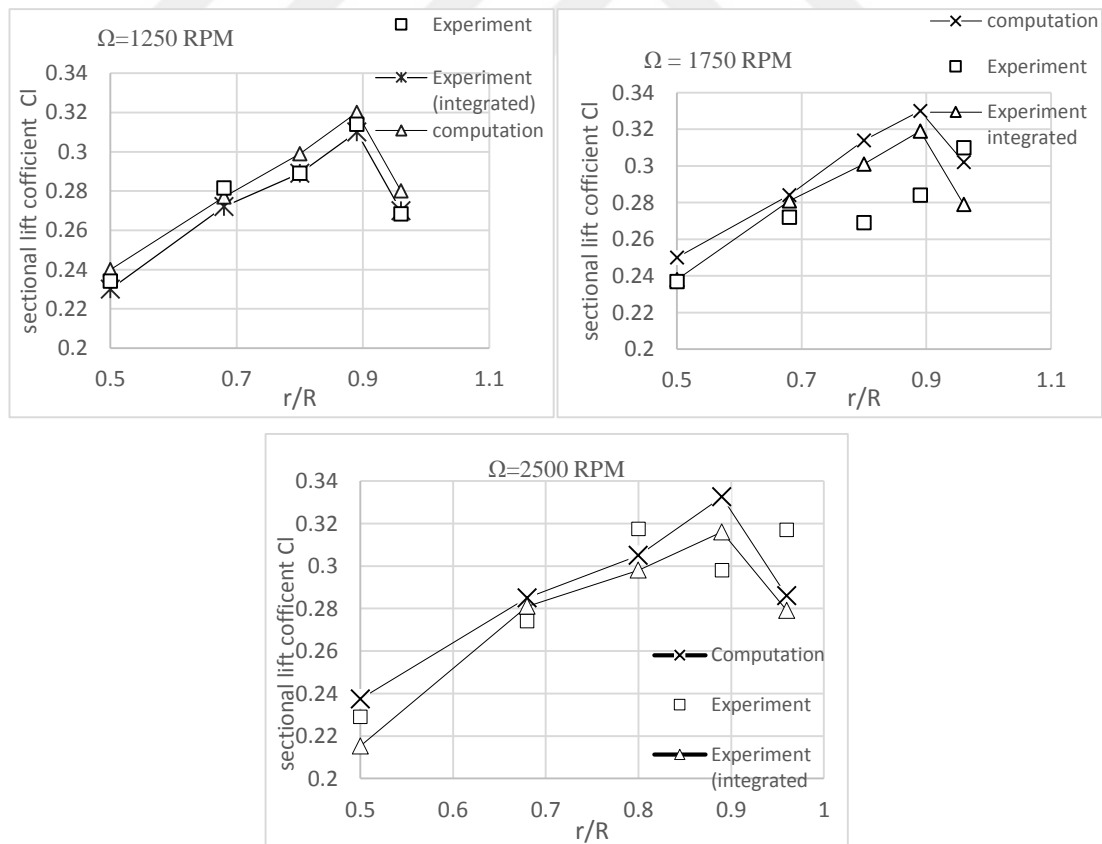


Figure 3. 18: Comparison of sectional lift coefficient for Cardonna-Tung

### 3.2.5 Validation Results at 5° Collective Pitch Angle

In this section, the distributions of pressure coefficient  $C_p$  at low collective pitch angle (5 degrees) and two rotational speeds of 1250 and 1750 rpm are computed and compared with the experimental data.

The outcomes for pressure coefficient exhibited reasonable agreement with the experimental data, and they are shown in the following graphs.

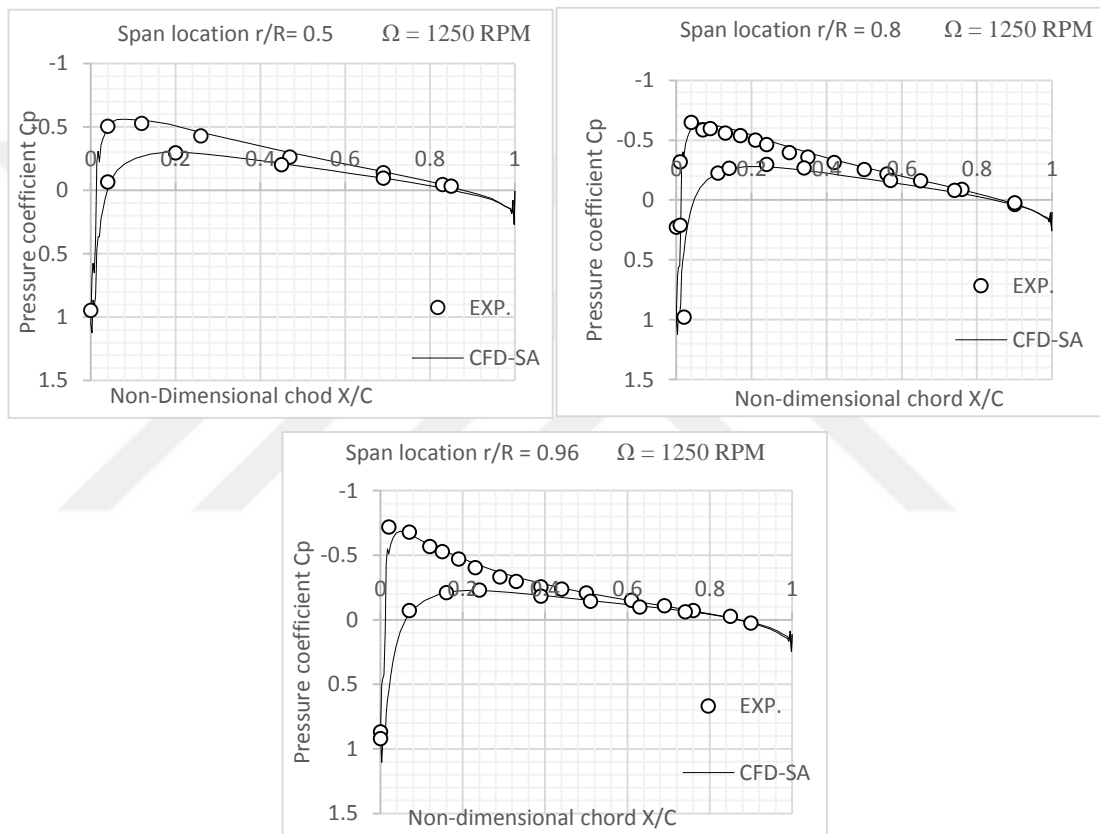


Figure 3. 19: Comparison between Numerical (SA) and experimental data at different span-wise sections on Caradonna–Tung at 1250 rpm at 5° collective angle

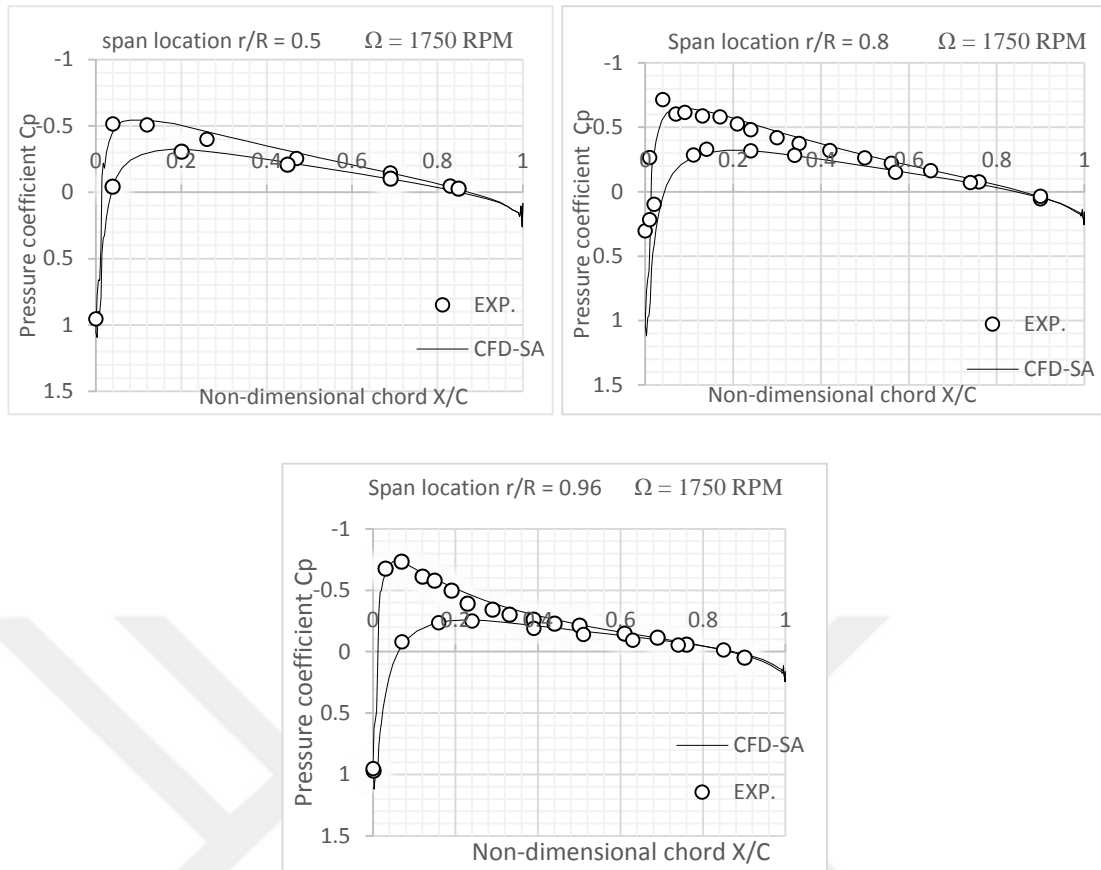


Figure 3. 20: Comparison between Numerical (SA) and experimental data at different span-wise sections on Caradonna–Tung at 1750 rpm at 5° collective angle

At collective angle of 8 degrees and at rotational speeds of 1250 rpm and 1750 RPM, the computed pressure distribution shows agreement with the experimental data at all blade sections, which is shown in Figures 3.15 and 3.16. At higher rotational speed of 2500 RPM, there was discrepancy between the experimental and the computed pressure coefficient distribution specially at the outboard span sections (80% and 96%). This happened because of the strong vortices at this high rotational speed as shown in Figure 3.11.

At 5 degrees and 1250 as well as 1750rpm rotation speeds, the calculated pressure coefficient distribution on all the blade sections showed good agreement with the experimental data, which is obvious in figures 3.19 and 3.20.

### 3.3 Test Case 2: UH-60A Black Hawk Helicopter Blade

In this case, the UH-60A Black Hawk helicopter rotor is used for validation. This rotor consists of four twisted blades with sweep. The UH-60A rotor has been extensively studied, and the results are given in many publications [58-63]. Besides experimental results, different research groups conducted several simulations.

In this study, both of the zero-thrust and the high-thrust cases of UH-60A are studied as shown in the following sections.

#### 3.3.1 Blade Description and the Experimental Data

Because of the flow-field periodicity, just a single blade was considered and the periodic boundary condition was implemented on the other blades.

The blade features and geometric dimensions were taken using a scale of (1: 5:73) as shown in [58].

The data was acquired for a 9:4ft 2.9 m diameter, four-blade scale (1: 5:73) of UH-60A rotor. A UH-60A rotor blade consists of two different airfoils distributed as follow: SC1095 airfoil in the root and tip regions and the SC1094R8 airfoil in the mid-span region as shown in Figure 3.20.

The mentioned blade possesses unique twist distribution as Figure 3.21 shows. The blade twist distribution has a linear shape as  $r/R < 0.75$  while it is non-linear on the tip. The blade has a built-in twist that linearly varies in the 80% blade radius, and it has hook-like non-linear twist closer to the tip, which is part of the model. Moreover, the blade's elastic twist applies the measured defections [58].

A blade pitch distribution having a built-in, collective, and elastic twist can be plotted against the radius and compared to the experimental results as shown in Figure3.22. In addition, there is also a 20° rearward sweep beginning at  $r/R = 0.93$ .

The average chord is 3.64in (0.0924m) that produces a 15:3 blade aspect ratio and 0.0825 solidity ratio.

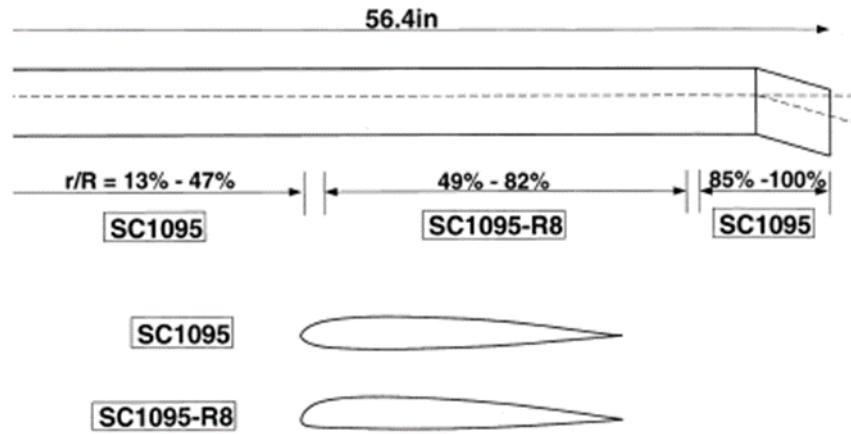


Figure 3. 21: Blade and airfoil shape of UH-60A black hawk rotor [63]

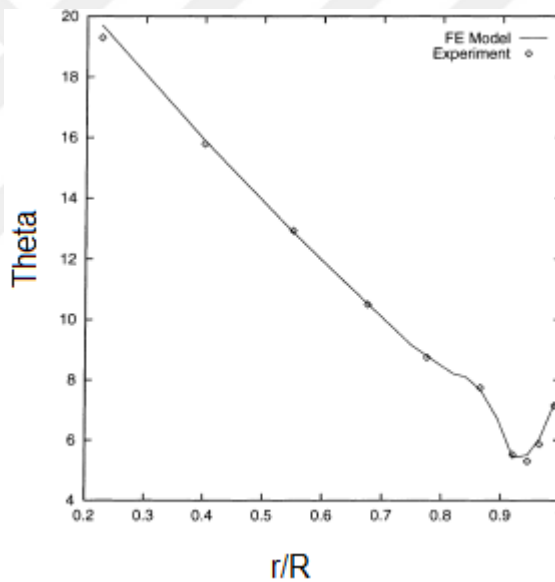


Figure 3. 22: The twist distribution of UH-60 blade [60]

We chose a couple of flow-field conditions for studying the CFD simulation solution procedure suitable for this blade. First, UH-60A blade was studied at zero thrust. The second case was studied at high thrust. Both the cases were compared with the experimental data. The description of both the cases has been summarized in Table 3.3.

Table 3. 3: UH-60A Black Hawk Blade Description for Both the Cases

Cases	At zero Thrust	At high Thrust
Two different airfoil sections	SC1095 – SC1094R8	
Number Of Blades	4	
Average Chord Length	0.0924 m	
Rotor Diameter	2.9 m	
Aspect Ratio	AR 15.3	
Ambient Pressure $P_{atm}$	101300 Pa	
Ambient Temperature $T_{atm}$	288.15 K	
Ambient Density $\rho_{atm}$	1.225 kg/m <sup>3</sup>	
Sweep at 92%	20 degrees	
Collective at $\theta$ 0.75 & coning $\beta$	-	10.47 & -2.31
Thrust coefficient $C_t/\sigma$	0.0	0.085
Rotor speed	1427 rpm	1425 rpm

### 3.4 Simulation and results for UH-60 blade in Hover Condition

#### 3.4.1 Geometric Blade

This case is different as compared to the first case because it contains two airfoils, which are asymmetrical, and besides, there is a twist and sweep back after 92%. The geometric blade was generated using AutoBlade software of NUMECA.

The collective pitch angle for the zero-thrust case is  $\theta$  0.75 = 0.11o and the cone angle is  $\beta$ =-20o while, the collective angle for the high-thrust case is  $\theta$  0.75= 10.47o and the corresponding cone angle is  $\beta$ = -2.31o. However, the chord length  $C = 0.0924m$  in both cases. The number of sections in the geometric blade was 17, which are mentioned in Table 3.4.

The 2D and 3D blade section shapes are shown in Figure 3.23.

Table 3. 4: Twist variations along the UH-60 rotor geometric blade at a high thrust value

No. of Section	Section location Hup ( m)	Span station r/R (r/1.432)m	Twist (degree )	Location of airfoil
1	0.186233	0.13	21.25794	SC1095
2	0.327069	0.228311	19.2586	
3	0.573459	0.400304	15.7608	
4	0.673303	0.47	14.41985	
5	0.701954	0.49	14.03505	SC1094R
6	0.787144	0.549467	12.8909	
7	0.963762	0.672755	10.4395	
8	1.105491	0.771689	8.75037	
9	1.174699	0.82	8.210038	
10	1.217676	0.85	7.874504	SC1095
11	1.236319	0.863014	7.72895	
12	1.289304	0.9	6.242261	
13	1.314453	0.917555	5.53662	
14	1.348976	0.941654	5.28749	
15	1.376232	0.96068	5.81066	
16	1.414389	0.987316	7.08122	
17	1.43256	1	7.08122	

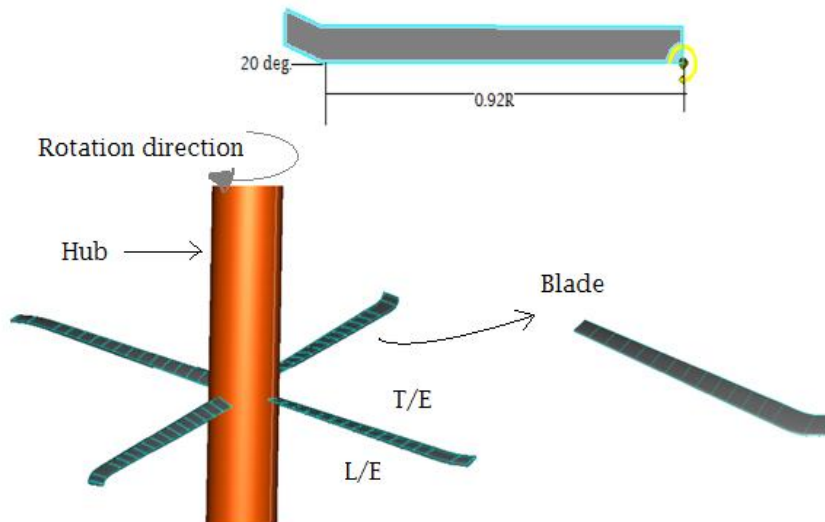


Figure 3. 23:3D UH-60A helicopter blade geometry drawn using AutoBlade

### 3.4.2 Mesh Generation

3D structured mesh was generated with the help of NUMECA AutoGrid mesh generator. The mesh for a single blade was generated with the periodic condition that artificially creates the conditions as if other blades are working. The entire mesh has around 9 million cells as shown in Table 3.5.

The thickness from the first grid point to the wall was estimated when  $V_{ref} = 213$  m/s,  $L_{ref} = 0.0924$  m and  $\nu = 1.7e-5$  m<sup>2</sup>/s.

Assuming that if we wish to get  $y^+$  around 1 at the wall, it turns out that  $Y = 2 \times 10^{-6}$  m. The range  $y^+$  is appropriate for the tested turbulence models.

Table 3. 5: Mesh quality of UH-60 Blade

Entire Mesh	8,939,898
Around the blade	5,724,243
Far Field	3,215,655

At mid-span, the 2D mesh of the blade has been illustrated in Figure 3.24, which has 16 blocks, and all of them stand together for the blade and the external field mesh. It has been illustrated in Figure 3.25.

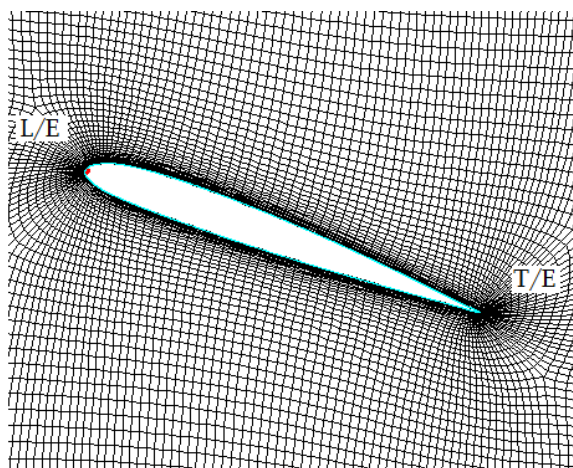


Figure 3. 24: The 2D mesh at blade mid-span of UH-60 helicopter rotor blade



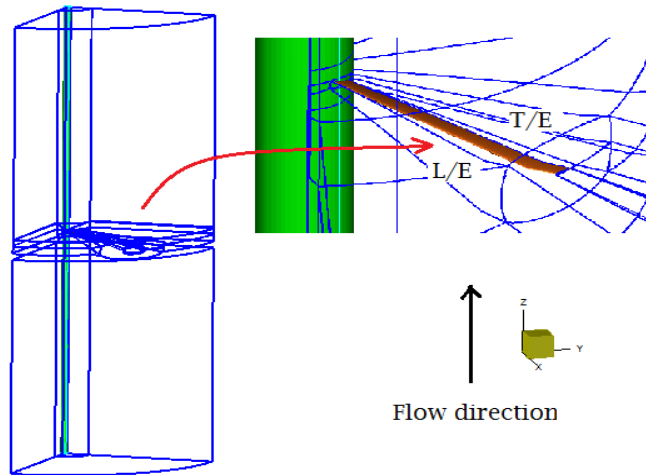


Figure 3. 25: The 3D mesh for UH-60 helicopter blade

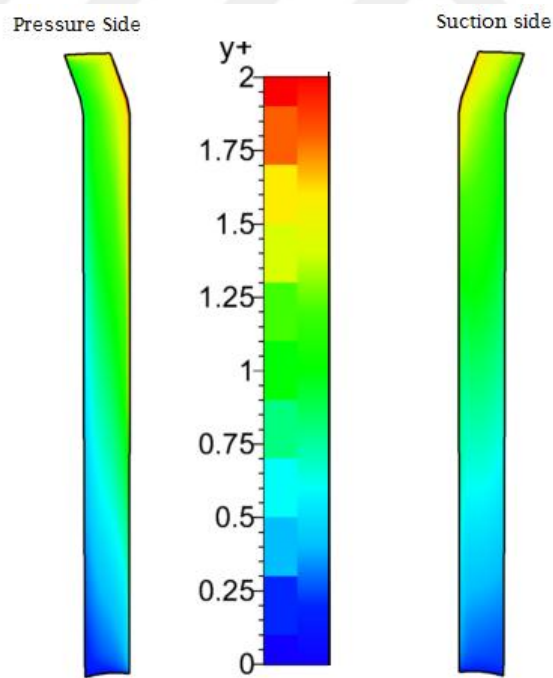


Figure 3. 26:  $y^+$  Value for UH-60A helicopter

### 3.4.3 Valuation Results of Two Cases

#### 3.4.3.1 At low Thrust $C_T / \sigma \approx 0.0$

After computations, both the pressure coefficient distributions were compared with the corresponding values available in the experimental data for the finer initial grid (8,939,898) at four spanwise blade sections such as 55%, 77%, 92% and 94.5% at 1427 rpm in Figure 3.27. The turbulence model used was the Spalart-Allmaras and the results were stored after 5000 iterations.

The computed pressure coefficient distribution of every blade section shows good agreement when the values were compared with the experimental data as Figure 3.27 shows.

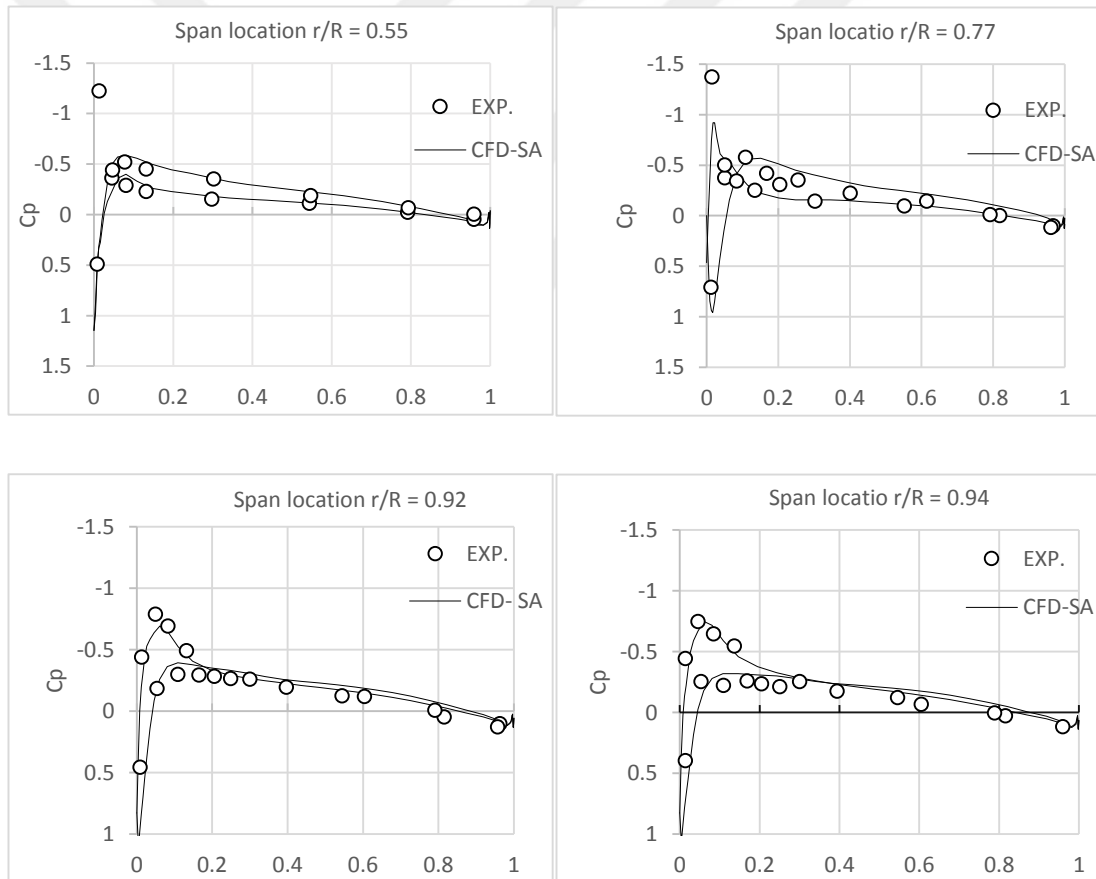


Figure 3. 27: Comparison between CFD and experimental data at different span-wise sections on UH-60A at 1427 rpm

The 3D gauge pressure contours on the pressure and suction sides of the UH-60 blade are illustrated in Figure 3.28.

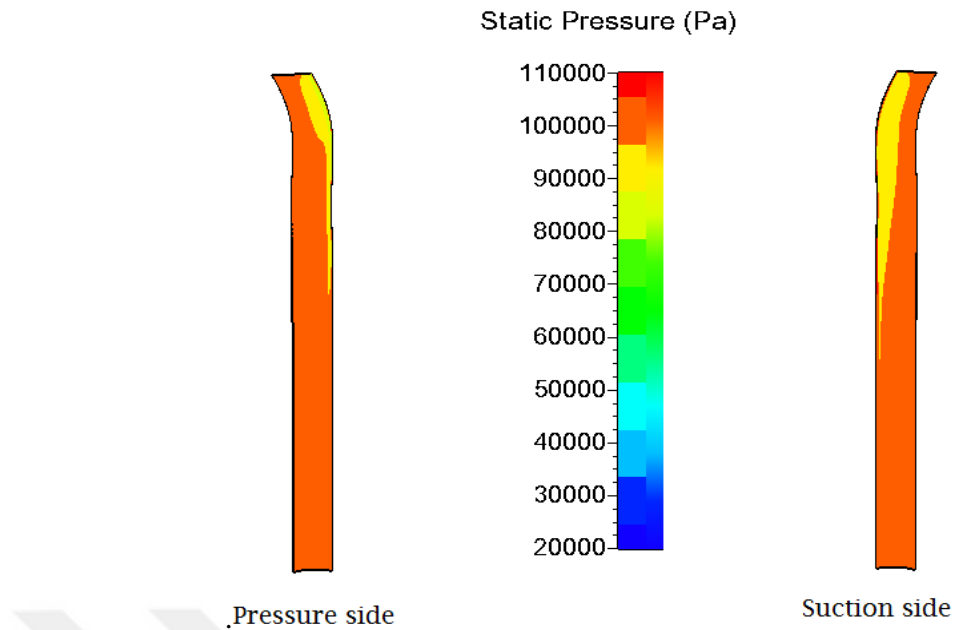


Figure 3. 28:Gauge pressure contours for UH-60A blade at 1427 rpm

### 3.4.3.2 Observations at high Thrust

Both the pressure coefficient distributions were compared with the experimental data for the finer initial grid at four span-wise sections of the blade 77.5%, 92%, 94.5%, and 96.5% at 1425 rpm. Again the results were stored after 5000 iterations.

In case of high thrust, a noticeable discrepancy exists between the experimental and computed pressure coefficient distribution both in the suction and pressure sides at the outboard span 94.5% and 96.5% have been illustrated in Figure 3.29. This is so because of strong vortices at high rotational speed; so, it causes large separation in the concerned section.

In case of sectional outboard span 77.5% and 92%, discrepancy exists (pressure side) between the experimental and computed pressure coefficient distributions.

The 3D gauge pressure contours on suction and pressure sides of UH-60 blade have been illustrated in Figure 3.30 using the Spalart-Allmaras turbulence model at 1425rpm rotational speed.

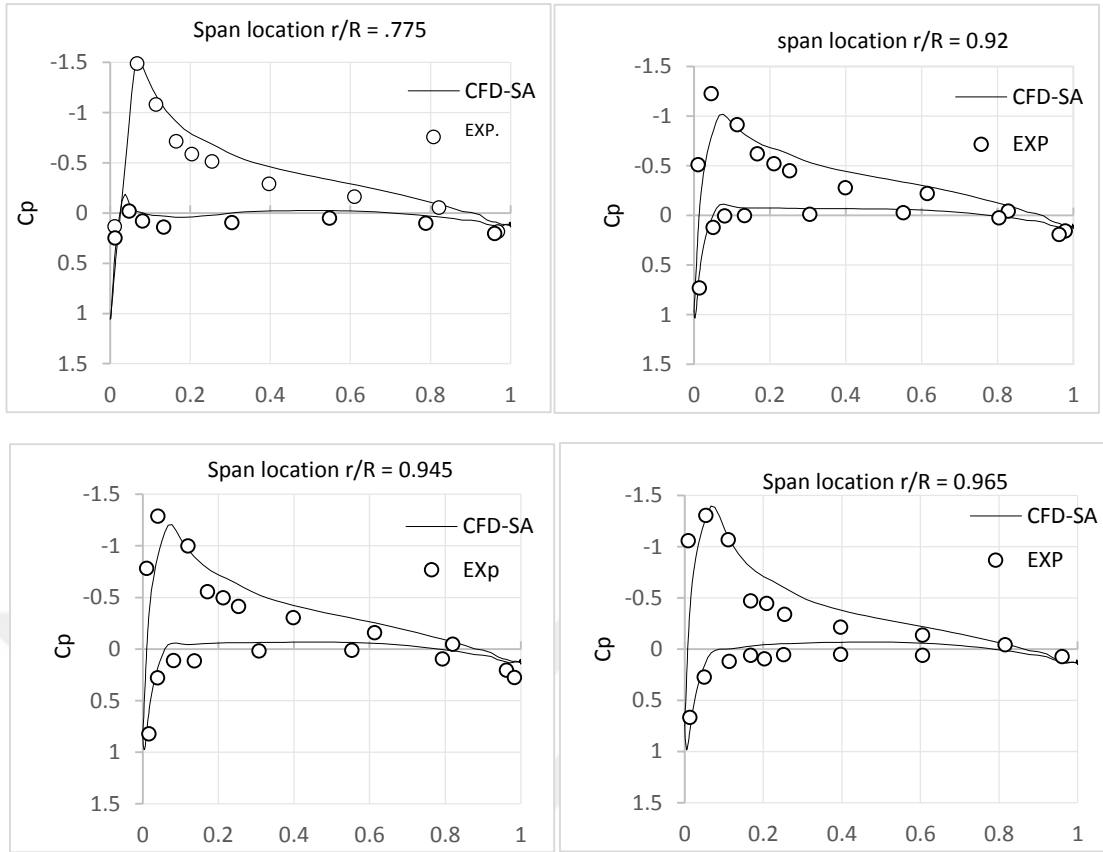


Figure 3. 29; Pressure coefficient distribution comparison between the Numerical (SA) and the experimental values at different span-wise sections for UH-60A blade at 1425rpm

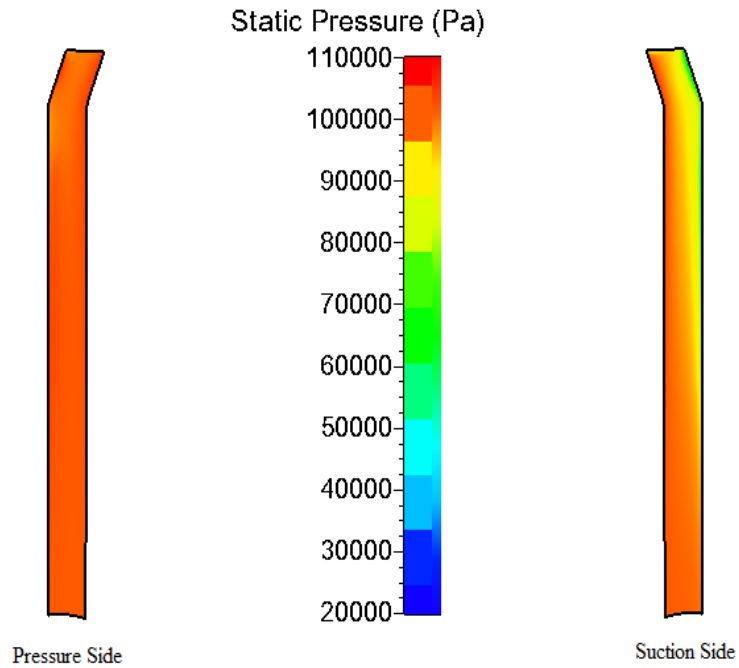


Figure 3. 30: Gauge pressure contours for UH-60A blade at 1425 RPM

## CHAPTER 4

### PARAMETRIC STUDY

As mentioned before, the Caradonna-Tung blade and the UH-60 Black Hawk helicopter blades were chosen for the parametric study. The shape of blade and its tip are significant for the helicopter's aerodynamic performance. The blade tips encounter the peak pressure and high Mach number while strong trailing tip vortices are produced. A poor tip design causes serious implications for the performance of a rotor. In this chapter, the changes in the shape of the blades will be discussed in three parts; first part will analyze the effect of the blades' sweepback angle on the thrust production of the rotor and how to improve the figure of merit of the rotor blade. The second segment will throw light on adding a winglet to the blade tip and study its impact on the rotor thrust and torque. The third segment will show the effect of a maple seed shaped blade on the trust production of the UH-60 black hawk helicopter rotor. All those studies are conducted under the hovering condition.

#### 4.1 Study of Sweep angle and location

Sweeping the leading edge of blade decreases the Mach number allowing the rotor to attain a higher advance ratio. The advance ratio is the ratio of the freestream speed to the rotor tip speed. This decreases the compressibility effects and hence decreases both of the drag and the need for net rotor power. Figure 4.1 shows the shape of the sweep angle.

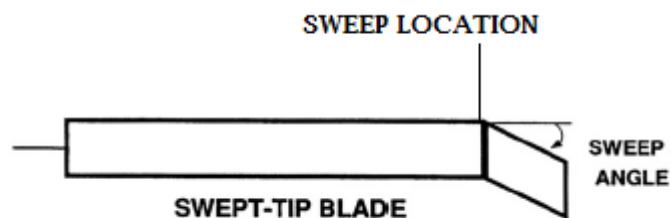


Figure 4. 1: Swept-back blade-tip

At Maryland, Chopra and Kim [65] analyzed the aero-elastic responses of various blade shapes such as rectangular, anhedral, UH-60 type blades, and tapered-tip blades. The use of sweep also affects the tip vortex formation, and its location after it has been trailing from the blade; however, there is a definitive impact of rotor-tip vortex formation issue as well as the impact of tip shape on the vortex characteristics including the velocity profile and the diffusive characteristics.

It is likely, however, that this area of research might lead towards improving the tip shapes and rotor blades, which were optimized for lower induced drag.

This chapter will throw light on different effects of sweep angle on the blade tip (backward) with different locations of sweep along with the blade span on the thrust production and improvement in the figure of merit.

#### 4.1.1 Sweep angle Configurations of the Caradonna – Tung Rotor blade

The tilting direction has been tested for many sweep configurations to find an ideal configuration to produce thrust.

Different location of sweep were considered; 80%, 90%, 92%, 94%, 95% and 96% spanwise at different sweepback angles 30, 40, 50, 60 and 80 degrees. Two cases are shown in Figure 4.2.

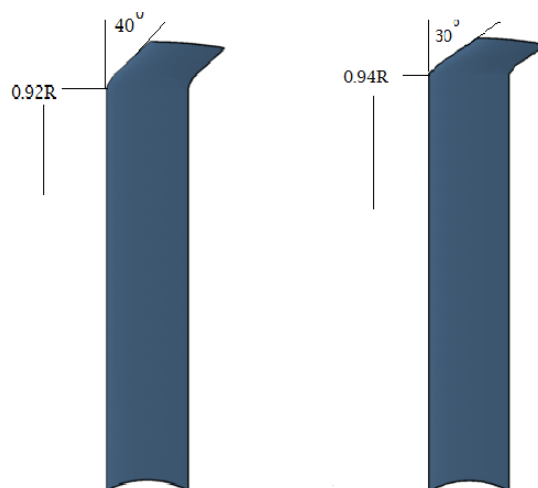


Figure 4. 2: Locational of sweep angle of 40 deg. And 30 deg. At 92% and 94%

#### 4.1.2 CFD Simulations During the Hovering Condition

We applied the mesh topology, which is used in Section 3.2 (shown in Figure 4.3) with the same RANS settings used for the flowfield computations of the baseline blade.

The analysis were carried out under three rotation speeds 1250, 1750 and 2500rpm at 8-degree collective pitch angle during the hovering condition.

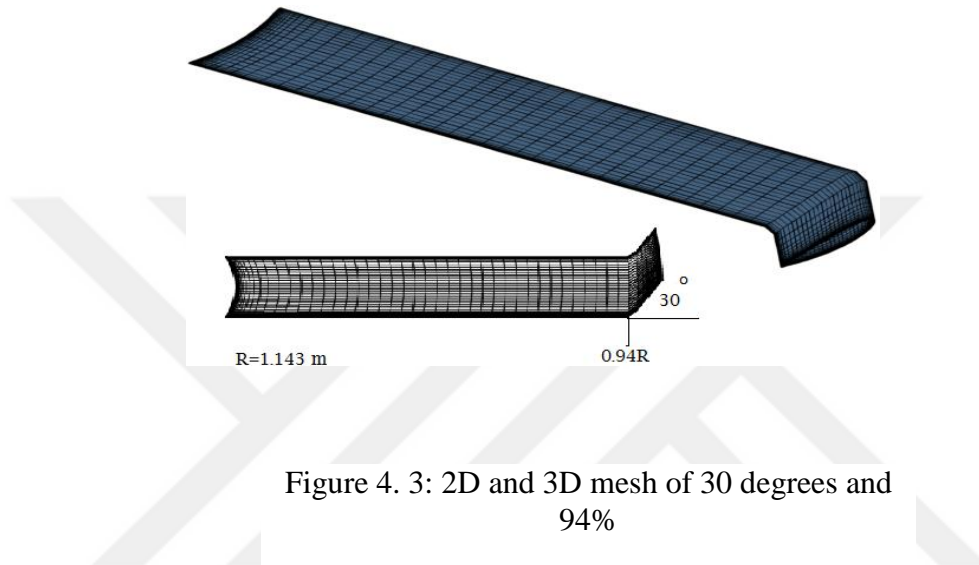


Figure 4. 3: 2D and 3D mesh of 30 degrees and 94%

Calculating the percentage of increase in thrust and the percentage of decrease in torque and also the figure of merit (FM) for sweepback angle configurations is significant in determining the rotor performance. The FM is an indication of both the thrust and torque as given in Equation 2.75. The helicopter rotor blade efficiency during the hovering condition is usually expressed in terms of FM.

Higher thrust generation is better for the hovering condition. However, more torque generation means that more power is needed to attain that thrust, which makes the helicopter less efficient.

The percentage of computed thrust increase and the torque decrease as compared to baseline blade geometry were obtained for each configuration at three rotational speeds 1250, 1750 and 2500rpm at 8-degree collective pitch angle. All the analysed cases are summarized in tables 4.1, 4.2 and 4.3.

Table 4. 1: The percentage of Thrust, Torque and FM for the different cases for rotational speed 2500 rpm

Sweepback angle	Sweep Location r/R	F.M	Increase Thrust (%)	Decrease Torque (%)
Baseline		0.368	0	0
30 degree	94%	<b>0.401</b>	0.760	<b>6.985</b>
	96%	0.394	0.253	6.123
40 degree	92%	<b>0.402</b>	<b>1.171</b>	6.551
	94%	0.398	0.984	6.049
	96%	0.390	0.228	5.169
50 degree	92%	0.395	1.034	5.268
	94%	0.392	0.673	4.880
60 degree	80%	0.369	-0.929	1.354
	90%	0.373	-3.091	5.572
	92%	0.388	0.587	4.083
	94%	0.385	0.231	3.914
	95%	0.381	-0.281	3.615
	96%	0.381	-0.284	3.615
80 degree	90%	0.375	-0.482	2.492
	94%	0.375	-0.649	2.591

Table 4. 2: The percentage of Thrust, Torque and FM for the different cases for rotational speed 1750 rpm.

Sweepback angle	Sweep Location r/R	F.M	Increase Thrust (%)	Decrease Torque (%)
Baseline		0.42	0	0
30 degree	94%	0.418	-1.648	1.898
	96%	0.419	-1.557	1.974
40 degree	92%	0.422	-1.374	2.354
	94%	0.422	-1.190	2.202
	96%	0.423	-1.282	2.354
50 degree	92%	0.424	-1.099	2.354
	94%	0.424	-1.007	2.354
60 degree	80%	<b>0.429</b>	-1.190	<b>3.721</b>
	90%	0.401	-5.403	3.417
	92%	0.425	-1.007	2.430
	94%	0.425	-1.007	2.430
	95%	0.424	-1.099	2.506
	96%	0.424	-1.190	2.582
80 degree	90%	0.425	-0.916	2.430
	94%	0.424	-1.099	2.506



Table 4. 3: The percentage of Thrust, Torque and FM for the different cases for rotational speed 1250 rpm.

Sweepback angle	Sweep Location r/R	F.M	Increase Thrust (%)	Decrease Torque (%)
Baseline		0.439	0	0
30 degree	94%	0.430	-1.784	0.615
	96%	0.431	-1.729	0.615
40 degree	92%	0.433	-1.636	1.077
	94%	0.435	-1.338	0.923
	96%	0.435	-1.431	1.077
50 degree	92%	0.436	-1.283	1.231
	94%	0.436	-1.190	1.077
60 degree	80%	<b>0.446</b>	-1.264	3.231
	90%	0.395	-9.126	<b>3.631</b>
	92%	0.437	-1.171	1.092
	94%	0.437	-1.152	1.077
	95%	0.437	-1.227	1.231
	96%	0.436	-1.264	1.154
80 degree	90%	0.438	-0.929	1.077
	94%	0.437	-1.190	1.123

It is obvious in the tables above that the sweep back angle at high rotational speeds has a greater and more pronounced effect as compared to the lower rotational speeds. In Table 4.1, at 2500rpm rotational speed, the best results for the efficiency of the blade are found in the case of 30-degree angle at 94% and 40-degree angle at 92%.

At his point, the thrust increase and torque reduction gave the best value of figure of merit. The minimum torque in this study at 2500 RPM was attained at sweptback of 30-degrees angle located at 94% span.

For this configuration the torque has decreased by around 7%. The effect of sweptback on the thrust is less pronounced. The maximum increase in thrust was only 1.2% above the baseline value.

At low rotational speeds such as 1250 and 1750rpm, we find the sweep back angle that has lower effect on the blade torque and thrust values. There was no increase in thrust but the torque has decreased by around 3%.

Table 4.4 provides the best cases of thrust and the figure of merit with the least torque that also shows the maximum value at all the rotational speeds.

Table 4. 4: Optimum Cases for thrust, torque and FM

RPM	Increase Thrust (%)		Decrease Torque (%)		FM	
	Angle	Span	Angle	Span	Angle	Span
1250	80 deg./90%	-0.929	60 deg./90%	3.63	60 deg./80%	0.445
1750	80 deg./90%	-0.916	60 deg./80%	3.721	60 deg./80%	0.429
2500	40 deg./92%	1.17	30 deg./94%	6.984	40 deg./92%	0.402

The pressure coefficient at different spanwise locations was plot for the sweptback angles of 30° and 40° located at 94% and 92% span respectively and compared with the baseline blade at 2500 RPM as shown in Figure 4.4.

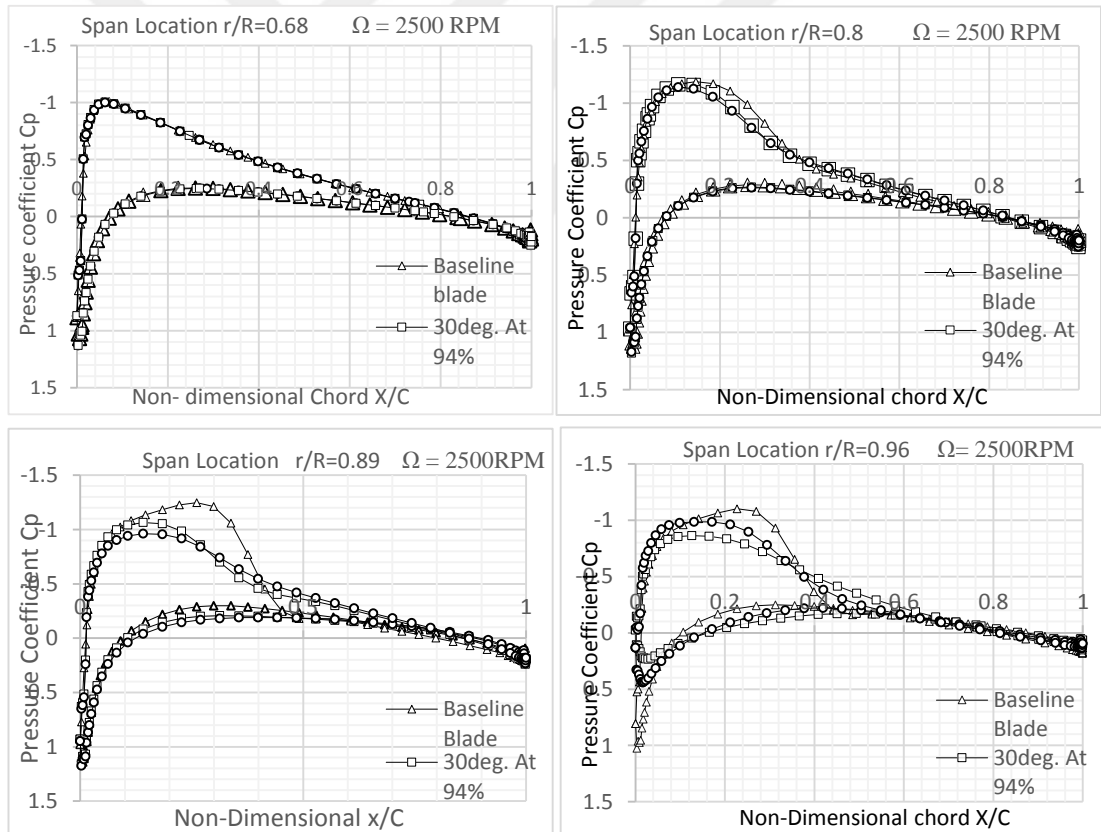


Figure 4. 4: Pressure coefficient distribution comparison between Baseline and Optimum Cases at different span-wise sections at 2500rpm and 8 degrees collective pitch angle.

At 2500 rpm, the pressure coefficient was found to be different as compared to the baseline blade. It was found that the pressure rose towards the suction, and was high on the pressure side as well, which resulted in higher relative thrust at the outboard blade in the direction of the tip region.

With changing pressure distribution, the thrust increased and the torque decreased, therefore, increase in the figure of merit was observed.

#### 4.1.3 Sweep angle Configurations of UH-60A

Different configurations were tested with different tilting directions in order to find the best thrust production configuration.

The baseline blade with the same geometry but different sweep locations (span-wise 80%, 90% 92% and 94%) were taken with different sweep angles (5, 10, 15, 20, 25 and 30 degrees) at the same collective pitch angle, as Figure 4.5 shows.

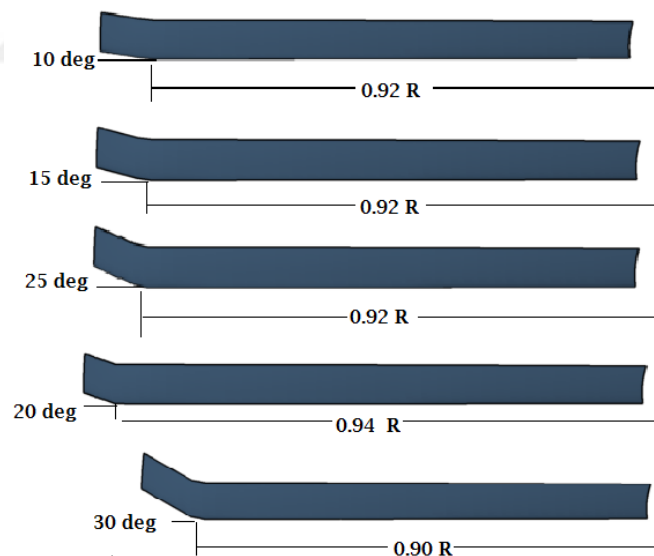


Figure 4. 5: Different sweep angles and sweep locationals of UH-60A

#### 4.1.4 CFD Simulations and Results of UH-60A

The mesh topology, which was used in Section 3.3, has been applied in this case. RANS equations were solved to find the results using the Spalart-Allmaras as a

turbulence model. These results are obtained at the rotation speed 1425rpm at Collective  $\theta_{0.75} = 10.47$  degrees and coning  $\beta = -2.31$  degrees.

Calculating the percentages of torque, thrust, and FM is important for finding increase/decrease that has taken place because of different sweep configurations.

The thrust and torque percentages, which were closer to the results of the original blade geometry, are given below:

Table 4. 5: The percentage of thrust, torque and figure of merit for different cases at the rotational speed 1425rpm

Sweepback Angle	Sweep Location r/R	F.M	Increase Thrust (%)	Decrease Torque (%)
0	0	0.730	-0.466	0.036
5 degree	90%	0.698	-0.699	-4.173
	92%	0.732	-0.513	<b>0.468</b>
	94%	0.733	-0.559	<b>0.540</b>
10 degree	90%	0.732	-0.466	0.288
	92%	0.709	-2.657	<b>0.468</b>
	94%	0.733	-0.466	0.432
15 degree	90%	0.735	0.047	-0.036
	92%	<b>0.736</b>	<b>0.047</b>	0.072
	94%	<b>0.737</b>	<b>0.047</b>	0.216
20 degree	90%	0.729	-0.466	-0.072
	<b>92%</b>	<b>0.735</b>	<b>baseline</b>	
	94%	0.731	-0.420	0.180
25 degree	90%	0.732	-0.093	-0.252
	92%	0.733	-0.047	-0.216
	94%	0.734	-0.093	0.000
30 degree	80%	0.734	<b>0.420</b>	-0.719
	90%	0.730	-0.233	-0.288

From the results mentioned above, there is a little change in the thrust and figure of merit for the different sweep and location angles.

## 4.2 Winglet Study

This study was started in July 1976, when Whitcomb [66 , 67], NASA Langley Research Centre published a study that mentioned some design approaches, which

briefly mentioned and explained the aerodynamic technology called as the winglet design.

The study mentioned that some little but vertically arranged fins should be installed on the KC-135A aircraft wings. They were tested during the years 1979 and 1980. The winglet was capable of carrying aerodynamic loads.

The vortex was caused when the winglet spread out that decreased the downwash, which resulted in further reduction in the induced drag as compared to the area increase in the profile drag.

Whitcomb proved that the tiny winglets had the capacity to raise an aircraft's range by up to 7% of the cruise speeds. This process reduced the induced drag and increased the profile drag when the airspeed increased.

In 1980s, a NASA contract [68] reassessed winglets as well as other drag reducing devices, and discovered that wingtip devices including winglet, sails and feathers were effective for improving drag as the lift efficiency increased 10-15% in case when those wingtip devices are integrated with the wing design.

Mark D. [69] proposed a new winglet design and predicted their performance (SAILPLANES) as they had good agreement with the results of the flight-test; however, the designs were tested for very limited time.

Monier ElFarra conducted a study [70], in which, he pointed out that if a winglet is added to a wind turbine blade, which points towards the blade's suction side; it will generate more power.

For understanding the process of reducing the drag with the help of the winglet, the difference between the induced drag and the profile drag must be understood.

The profile drag takes place because of the viscosity caused by the air that moves on the airfoil surface and also because of the pressure drag. When the wind turbine blades move in that viscous air, some air sticks to the blades while the remaining continues its motion. The air requires the blade's energy to rotate with the blade, so when this energy transfers from the blade to the air, it causes the profile drag. Moreover, some other factors also result in the profile drag such as the blade's wetted area, the attack angle and the blade's airfoil shape [71 and 72].

The induced drag also occurs because of the lift caused by the blade. When the lift exists, the blade sides should have pressure difference. These sides are distinguished based on the pressure such as the pressure side and the suction side (lower pressure side). The pressure difference causes span-wise flow from the pressure side towards the suction side, which can be felt all along the trailing edge because the flow that leaves the suction side shifts inwards. On the other hand, the flow coming from the pressure side shows an outward movement. These are two opposing flows but when they meet each other on the trailing edge, their collision results in a swirling motion, which is concentrated on the known tip vortices. The vortices are generated with the help of energy, which transfers from the blade to the air. This energy transfer is called as induced drag that can be decreased when the span-wise flow is reduced. The winglets help reducing it [66].

When a winglet is added to a helicopter blade, it produces a flow that opposes the airflow generated by the blade. Hence, it cancels or at least weakens the blade's main flow reducing the spanwise flow, which, consequently, reduces the induced drag. A winglet's function is to diffuse the tip vortex effect; so, it decreases the induced drag; however, adding a winglet increases the wetted area that further increases the profile drag.

Every wing designer should focus on reducing the induced drag but for that, he/she should first assure minimum/negligible profile drag increase. A majority of commercial aircraft designs include winglets for reducing the induced drag; so, it helps saving fuel. Interestingly, birds have this feature that helps them fly but their winglets (tiny feathers) are not fixed; however, the winglet is fixed in conventional aircrafts.

It is possible to design a winglet in many geometrical shapes/variations, which might result in optimizing the aerodynamic efficiency of a wing during varying flight conditions in addition to reducing fuel consumption and pollution.

#### **4.2.1 Geometrical shapes for a Winglet**

For adding a winglet, the blade tip is 92% extended with respect to the blade radius, and then, it is tilted at different angles (10, 20, 30, 40, 50 and 80 degrees). The direction of the tilting angle and the winglet direction are very significant. For finding ideal winglet configuration for maximum thrust production, nine configurations were

tested. The configurations of the 9 cases are shown in Figure 4.3. Table 4.6 shows the winglet classification and results in CFD.

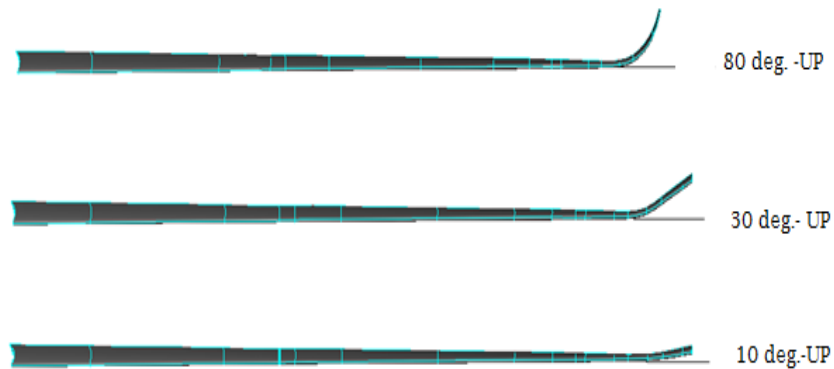


Figure 4. 6: Different winglet configurations

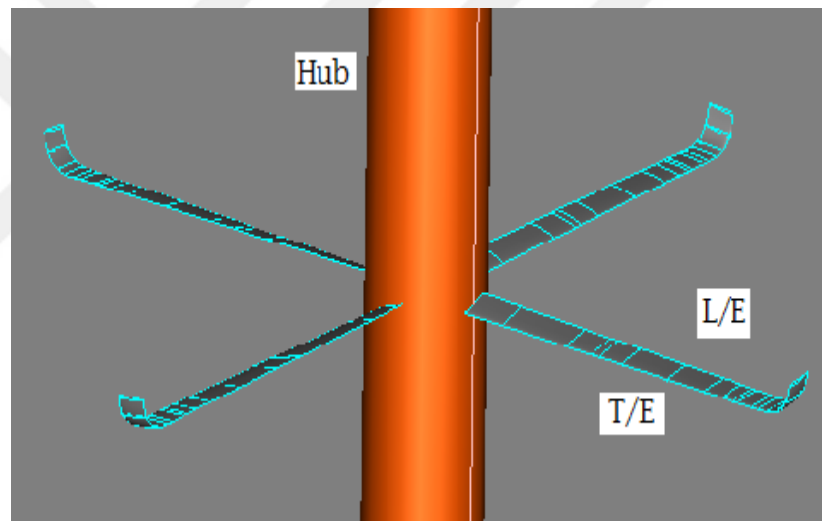


Figure 4. 7: Winglet at 80 degrees in case of UH-60A

#### 4.2.2 CFD Simulations and Results

Just like the sweep study and the mesh topology applied in Section 3.3, the RANS equations were solved to obtain the results using Spalart-Allmaras as a turbulence model. The results are obtained for the rotation speed 1425rpm at Collective  $\theta_{0.75} = 10.47$  degree and coning  $\beta = -2.31$  degree.

Calculating figure of merit increase is important because that happens because of varying winglet configurations, and it also helps calculating the thrust increase/increment percentage as well as torque reduction percentage for comparing

results with the original blade geometry. Every considered configuration has been listed in Table 4.6.

Table 4. 6: The percentage of Thrust, Torque and Figure of Merit for the different cases at 1425 rpm rotational speed

Cant angle (deg.)	FM	Increase Thrust (%)	Decrease Torque (%)
10-up	<b>0.742</b>	<b>1.911</b>	-1.906
20-down	0.722	0.000	<b>-1.763</b>
20-up	<b>0.740</b>	<b>2.051</b>	-2.338
30-down	0.693	-1.538	-3.633
30-up	0.721	1.678	-4.424
40-up	0.720	1.399	-4.137
50-up	0.705	1.305	-6.259
80-down	0.588	-5.734	-14.424
80-up	0.649	0.886	-14.676

It is clear from the previous table that using a winglet of 20-deg tilted towards the upper surface increases the thrust by around 2% and at the same time the torque decreased by 2.3 %. For this case, the chord distribution along the span of this winglet has been changed to see the effect of winglet taper ratio on the rotor performance.

Table 4. 7: Compared between untapered and tapered winglet

Cases	Thrust (N)	Torque (N.m)
Untapered	2189	284.5
Tapered	1915	331.8

It is noticed that, the tapered winglet has degraded the rotor performance as it has increased the torque by about 16 % and decreased the thrust by around 13 %.

### 4.3 A Study on Maple-shaped Blade

Maple shape or samaras are interesting specimens for a biological aerodynamic study. It is not just an interesting exercise to analyze and understand the computational fluid dynamics but this investigation on the autorotation of maple seed-shaped blade



gave new insights and unique exposure to the wind. This design is very important for designing wind turbines, biomimicry, and renewable energy technology.

Biomimicry is a science of finding suitable solutions of the technological problems through finding solutions from the nature including both plants and animals by using their shapes and mimicking their geometry in real life [73].

#### 4.3.1 Maple shape configuration of UH-60

Maple shape is made by tilting the blade at different angles (10, 20, 30, 40 and 50 degrees) as well as turning the wings in the direction of the towards the trailing edge of the blade. In addition to that, there is no sweep angle blade for the purpose of obtaining maximum thrust and minimum torque. The following shapes illustrate the geometric shape of the maple-shaped blades.

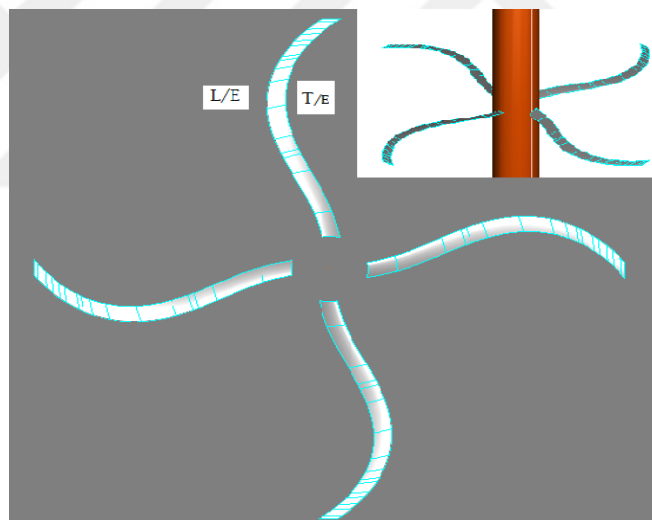


Figure 4. 8: Maple shape at 50 degrees

#### 4.3.2 CFD Simulations and Results

For this study, a similar mesh girt was used, which was utilized for the previous cases of UH-60 as well as the one, which was used for solving the RANS equations with the help of Spalart-Allmaras as a turbulence model.

The results have been obtained at 1425rpm rotational speed at  $10.47^\circ$  collective angle. Table 4.8 shows the percentages of thrust, torque and FM of different cases at 1425rpm rotational speed.

Table 4. 8: The percentage of Thrust, Torque and Figure of Merit for the different cases at 1425rpm rotational speed

Angle-maple	FM	Increase Thrust (%)	Decrease Torque (%)
maple-10-TE	<b>0.737</b>	1.865	-2.446
maple-20-TE	<b>0.736</b>	1.445	-1.978
maple-30-TE	0.733	0.233	-0.540
maple-40-TE	0.713	-2.191	0.360
maple-50-TE	0.717	-5.361	5.612

The results given above clearly indicate that placing the maple shape at 10 degrees gives the best shape that increases thrust and provides the best figure of merit value at 10 and 20 degrees but the 50-degree angle gives the desirable low torque value.

In this chapter, the parametric of untwisted and un-tapered blade of Cardonna-Tung helicopter was tested at rotational speed 2500rpm at 8 degrees pitching angle with a twisted and un-tapered blade of UH-60A rotors at high thrust using CFD predictions. The parametrics included sweepback angle, location sweep angle, addition of a winglet, and creation of maple shape, after which, the detailed analysis of the actions of aerodynamic forces on a blade was carried out. Some specific observations are listed below.

The effects of the sweepback angle on pressure distribution and the efficiency of blade for Cardonna-Tung were compared with the results of the original blade at different span-wise sections. The effects were very clear at a high rotation speed. The effects of the parametric sweepback angle at 92% span-wise direction, winglet and maple shape were small on the UH-60 rotor helicopter because the blade of UH-60 already has the optimum design.

## CHAPTER 5

### CONCLUSIONS AND RECOMMENDATIONS

#### 5.1 Concluding Remarks

This study focuses on the parametrics of two blades (twisted and untwisted) for a helicopter rotor blade using CFD for more thrust and maximum figure of merit/minimum torque. During the study, many issues were considered and analyzed.

Mash study, Cardonna-Tung blade and UH-60A Black Hawk helicopter blade for validation, Turbulence models, Different sweep back angle and location sweep, different winglet, and maple shape blades configurations.

Based on the parametric study outcomes and other important factors, the following conclusions have been reported:

At first, three levels of grid resolution were evaluated for Cardonna-Tung. The number of grid points for coarse, fine and finer grids was approximately 131 thousand, 965 thousand, and 7 million respectively, so, it requires robust code to assure good agreement with correct results. Most results were used on the fine grid of the rotor blade because they were close to the real outcomes.

Investigations were focused on two test cases to check the validity of the RANS solver. Those tests were conducted on Cardonna-Tung and UH-60A Black Hawk. Their validation was tested through different turbulence models. The Spalart-Allmaras one-equation model has given better results in comparison with the other models in both the test cases. In fact, the SST two-equation model was expected to give better results because it combines the advantages of the K- $\epsilon$  and the SA models. The results showed agreement with previous conclusions/results. The Spalart-Allmaras (SA) model can accurately predict the thrust as compared to the SST model. For assessing this issue, the study of several different meshes was conducted, and this was mentioned at the beginning of the section; however, the Spalart-Allmaras (SA) was found to be sufficiently accurate and suitable for selection as a turbulence model to carry out further calculations and a parametric study.

The RANS solver was used to compare the computed pressure coefficient distribution for two cases using the experimental data. It was noticed that for all the rotational speeds, the results were close to the experimental data with the exception of small deviation on LE on the blade's pressure side for both the cases at a high speed. When the rotation speed exceeds the stall value, it increases the deviation specifically pertaining to the blade's pressure side at the place of vortices formation. These vortices have more strength closer to the root; so, great deviation exists between the computed and measured data in the location closer to the root. The computational results for both the pressure coefficient and the sectional lift coefficient at three rotation speeds showed reasonable agreement with the experimental data.

Many parametric configurations have been proposed in the study including sweep angle, location sweep, winglet and maple-shaped blade for Cardonna-Tung and UH-60A Black Hawk helicopter. The results of these experiments were compared with the original blade results. It was noticed that adding a sweep back angle and location to the Cardonna -Tung blade, or creating its shape that points towards the direction of the flow resulted in greater thrust and better value of figure of merit at high rotational speed. The effect of sweepback angle, winglet pointing towards the suction side and maple-shaped UH-60A blades were tested for thrust. Experiments show that the mentioned changes had a small impact on the thrust production, torque and figure of merit indicating that the UH-60A blade has an ideal design.

## **5.2 Recommendations and Future Work**

Recommendations:

Studies should be conducted on other parameters of Cardona –Tung helicopters including the twist-linear blade Cardonna-Tung and Winglet design. The thrust largely depends on the twist angles, and they are a very important parameter.

## REFERENCES

- [1] Gessow, Alfred and Myers, Garry C., Jr. "Aerodynamics of the Helicopter." New York: Macmillan Company, 1952.
- [2] J. Gordon Leishman, "Principles of Helicopter Aerodynamics", Second Edition, Cambridge University Press.
- [3] McCormick, Barnes W. Aerodynamics, Aeronautics and Flight Mechanics. New York: John Wiley & Sons, 1995.
- [4] Gunston, Bill and Spick, Mike. "Modern Fighting Helicopters". New York: Crescent Books, 1986.
- [5] Johnson, W. "Helicopter Theory", Princeton University Press, Princeton, New Jersey, US, 1980.
- [6] Leishman, J.G. "Principles of Helicopter Aerodynamics", Cambridge Aerospace Series, New York, NY, US, 2006.
- [7] Leishman, J. G. and Beddoes, T. S., "A semi-Empirical Model for Dynamic Stall", Journal of the American Helicopter Society, Volume 34, pp. 3-17, 1989.
- [8] Leishman, J.G. and Rosen, K.M. "Challenges in the aerodynamic optimization of high-efficiency proprotors", J American Helicopter Society, January 2011, 56, (1), pp 12004-1200421.
- [9] Droandi, G. "Wing-Rotor Aerodynamic Interaction in Tiltrotor Aircraft", PhD thesis, Politecnico di Milano, 2014.
- [10] Gur, O. and Rosen, A. "Comparison between blade-element models", Aeronaut J, December 2008, 112, (1138), pp 689-704.

- [11] Liu, J., Paisley, D. J. and Hirsh, J. "Tiltrotor Aerodynamic Blade Design by Numerical Optimization Method", American Helicopter Society Aerodynamics 46th Annual Forum, Washington, DC, US, May 1990.
- [12] G. Droandi , G. Gibertin "Aerodynamic shape optimisation of a proprotor and its validation by means of CFD and experiments", The Aeronautical Journal O October 2015 Volume 119 No 1220.
- [13] Harrington, R. D., "Full-Scale-Tunnel Investigation of the Static Thrust Performance of a Coaxial Helicopter Rotor," NACA TN-2318, March, 1951.
- [14] Dingeldien, R. C., "Wind-Tunnel Studies of the Performance of Multirotor Configurations," NACA TN-3236, August, 1954.
- [15] Leishman, J. G., Syal, M., "Figure of Merit Definition for Coaxial Rotors," Journal of the American Helicopter Society, Vol. 53, No. 3, pp. 290–300, 2008.
- [16] Leishman, J. G., "Principles of Helicopter Aerodynamics, Cambridge "University Press, New York, 2000.
- [17] Nili P. Gold and Mahendra J. Bhagwat," Rotor Hover Performance and Flowfield Measurements with Untwisted and Highly-twisted Blades", U. S. Army Research, Development, and Engineering Command (AMRDEC), Moffett Field, CA 94035.
- [18] Egolf, T.A., and Sparks, S.P., "A Full Potential Flow Analysis with Realistic Wake Influence for Helicopter Rotor Airload Prediction," NASA CR-4007, 1987.
- [19] Agarwal, R.K., and Decse, J.E., "Euler Calculations for a Flow field of a Helicopter Rotor in Hover," Journal of Aircraft, Vol. 24, No. 4, April 1987, pp. 231-238.
- [20] Mustafa D, Mark S. S, Joseph E. F, Kenneth J," Adaptive CFD analysis for rotorcraft aerodynamics", Scientific Computation Research Center, Rensselaer Polytechnic Institute, Troy, NY 12180, USA,1999.

[21] Potsdam M, Yeo W, Johnson W. ,“Rotor airloads prediction using loose aerodynamic structural coupling.American Helicopter “,Society 60th Annual Forum, Baltimore, MD, 7–10 June 2004.

[22] Holst, T. L. and Pulliam, T. H., “Overset Solution Adaptive Grid Approach Applied to Hovering Rotorcraft Flows,” AIAA Paper 2009-3519, June 2009.

[23] Strawn, R.C., and Ahmad, J., “Computational Modeling of Hovering Rotors and Wakes,” 38th AIAA Aerospace Sciences Meeting and Exhibit, Reno, NV, 10-13 anuary 2000, AIAA Paper 2000-0110.

[24] Pomin H, Wagner S. “Navier–Stokes analysis of helicopter rotor aerodynamics in hover and forward flight”. Journal of Aircraft 2002; 39(5):813–821.

[25] Juho Ilkko, Jaakko Hoffren and Timo Siikonen,” Simulation of a helicopter rotor flow”, Journal of Structural Mechanics, Vol. 44, No 3, 2011, pp. 186 – 205.

[26] Chen CL, McCroskey WJ, Obayashi S.” Numerical solutions of forward-flight rotor flow using an upwind method”. Journal of Aircraft 1991; 28(6):374 –380.

[27] Schmitz, S., Bhagwat. M., Moulton, M.A., Caradonna, F.X., and Chattot, J.J., \The Prediction and Validation of Hover Performance and Detailed Blade Loads," Journal of the American Helicopter Society, Vol. 54, No. 3, July 2009.

[28] Piotr Doerffer and Oskar Szulc,” Numerical Simulation Of Model Helicopter Rotor In Hover”, Institute of Fluid-Flow Machinery PAS, Fiszerza 14, 80-952 Gdansk, Received 28 May 2008.

[29] Hamid Farrokhfal, Ahmad Reza Pischevar,”A New Coupled Free Wake-Cfd Method For Calculation Of Helicopter Rotor Flow-Field In Hover”, J. Aerosp. Technol. Manag., São José dos Campos, Vol.6, No 2, pp.129-147, Apr.-Jun., 2014.

- [30] Elfarra M., Kaya M., & Kadioglu F., (2018) “A Parametric CFD Study for the Effect of Spanwise Parabolic Chord Distribution on the Thrust of an Untwisted Helicopter Rotor Blade”, 2018 AIAA Aerospace Sciences Meeting, 8–12 January 2018, Kissimmee, Florida.
- [31] F.X. Caradonna, C. Tung, Experimental and analytical studies of a model helicopter rotor in hover, NASA TM 81232, 1980.
- [32] Nik Ahmad Ridhwan Nik Mohd and George N. Barakos, “Computational Aerodynamics of Hovering Helicopter Rotors,”  
Jurnal Mekanikal, No 34, June 2012, pp. 16-46
- [33] M. Imiela, “High-fidelity optimization framework for helicopter rotors”,  
Aerosp. Sci. Technol. 23(1) (2012) 2–16.
- [34] M. Imiela, G. Wilke, “Passive blade optimization and evaluation if off-design conditions”, in: The 39th European Rotorcraft Forum, Moscow, Russia, September 2013.
- [35] A. LePape and P. Beaumier. “Numerical optimization of helicopter rotor aerodynamic performance in hover”, In 31st European Rotorcraft Forum, September 2005.
- [36] N.A. Vua, and J.W. Leeb, “Aerodynamic design optimization of helicopter rotor blades including airfoil shape for forward flight,” Vol. 42, 2015, pp. 106–117.
- [37] Ki-Chung Kim and Indeqit Chopra,” Aeroelastic Analysis of Swept, Anhedral, and Tapered Tip Rotor Blades”, University of Marglatld, Apr 1990.
- [38] Seokkwan Yoon, Thomas H. Pulliam, and Neal M. Chaderjian,” Simulations of XV-15 Rotor Flows in Hover Using OVERFLOW”, Conference; San Francisco, CA; January 22-24,2014.



- [39] Yashwanth Ram Ganti,” CFD Analysis of a Slatted UH-60 Rotor in Hover”, Associate Professor James D. Baeder Department of Aerospace Engineering, Master of Science, 2012.
- [40] Shinoda, P.M., Yeo, H., and Norman, T.R., “Rotor Performance of a UH-60 Rotor System in the NASA Ames 80-by 120-Foot Wind Tunnel,” Proceedings of the 58th Annual American Helicopter Society Forum, Montreal, Canada, June 11-13, 2002.
- [41] Seongim Choi, Kihwan Lee, Mark M. Potsdam and Juan J. Alonso, “Helicopter Rotor Design Using a Time-Spectral and Adjoint-Based Method,” Journal Of Aircraft, Vol. 51(2), 2014, pp. 412-423.
- [42] Stephen B. Pope, “Turbulent Flows”, Cambridge University Press, 2000.
- [43] David C. Wilcox, “Turbulence Modeling for CFD”, DCW Industries, Inc., 1993.
- [44] C. J. Chen, S. Y. Jaw, “Fundamentals of Turbulence Modeling”, Taylorand Francis, 1998.
- [45] Spalart P.R., Allmaras S.R., “A One-Equation Turbulence Model for Aerodynamic Flows”, AIAA 92-0439, AIAA 30th Aerospace Sciences Meeting and Exhibit, Reno, NV, Jan 6-9, 1992.
- [46] Klaus A. Hoffmann, Steve T. Chiang, “Computational Fluid Dynamics”, Volume III, Engineering Education System, Wichita, Kansas, 4th Edition, 2000.
- [47] Menter, F.R., “Two-Equation Eddy-Viscosity Turbulence Models for Engineering Applications”, AIAA Journal, Vol. 32, No. 8, pp. 269-289, 1994.
- [48] Launder B.E. and Spalding D.B., “The numerical computation of turbulent flow”, Comput. Methods App. Mech. Eng., vol. 3, pp. 269-289, 1974.
- [49] E. F. Toro, “Riemann Solvers ad Numerical Methods for Fluid Dynamics”, Springer, 2nd Edition, 1999.

[50] [http://www.cfd-online.com/Wiki/Sutherland\\_law](http://www.cfd-online.com/Wiki/Sutherland_law), Last Visited 13-August- 2010.

[51] Srinivasan, G. R., and Baeder, J. D., "TURNS: A Free-wake Euler/ Navier-Stokes Numerical Method for Helicopter Rotors," AIAA Journal, Vol. 31, No. 5, May 1993, pp. 959{961.

[52] Aly S., Marconi F., Ogot M., Pelz R., Siclari M., "Stochastic Optimization Applied To CFD Shape Design", AIAA-95-1647-CP, pp. 11-20, 1995.

[53] Seddon J. Basic Helicopter Aerodynamics (1st edn). BSP Professional Books: Oxford, 1990.

[54] NUMECA International. AutoBlade Software Package, ver.11.2rc, User Manual, 2017.

[55] NUMECA International, FINETM/Turbo Software Package, ver.11.2rc, User Manual, 2017.

[56] NUMECA International. IGGTM/AutoGrid5TM Software Package, ver.11.2rc, User Manual, 2017.

[57] P. F. Lorber. "Aerodynamic Result of a Pressure-Instrumented Model Rotor Test at the DNW". United Technologies Research Center East Hartford, Conn., USA, 1991.

[58] M. Dinar, A. Leminos and M. Shephard. "Adaptive Solution Procedures for Rotorcraft Aero-dynamics." Rensselaer Polytechnic Institute, Rotorcraft Technology Center, Troy, NY, USA,1997.

[59] M. Potsdam, H. Yeo and W. Johnson "Rotor Airloads Prediction Using Loose Aerodynam- ical/Structural Coupling." American Helicopter Society 60th Annual Forum, Army/NASA Rotorcraft Division Aeroflightdynamics Cirectorate (AMRDEC) U.S. Army Research, De-velopment, and Engineering Command, Moffett Field, CA, USA, 2004.

[60] M. Potsdam, H. Yeo and W. Johnson. "Rotor Airloads Prediction Using Loose Aerodynamic/Structural Coupling." *Journal of Aircraft* 3(43):732 - 742,2006.

[61] A. Datta. "Fundamental Understanding, Prediction and Validation of Rotor Vibratory Loads in Steady Level Flight." Doctoral Thesis, University of Maryland, College Park, MD, USA, 2004.

[62] UH-60 Airloads Program Tutorial.

<http://rotorcraft.arc.nasa.gov/tutorial/index.html#0>. 2011.

[63] W. G. Bousman. "Aerodynamic Characteristics of SC1095 and SC1094 R8 Airfoils." NASA TP-2003-212265, Aeroflightdynamics Directorate U.S. Army Research, Development, and Engineering Command Ames Research Center Moffett Field, CA, USA, 2003.

[64] Hirsch, C., "Numerical Computation of Internal and External Flows," Volume 2," Wiley Publishers, 1990.

[65] KimK-C, ChopraI. "Aeroelastic analysis of swept, anhedral, and tapered tip rotor blades". *Journal of the American Helicopter Society*1992;37(1):15–30.

[66] Whitcomb R.T., "A Design Approach and Selected Wind-Tunnel Results at High Subsonic Speeds for Wing- Tip Mounted Winglets", NASA TN D-8260, July 1976.

[67] Whitcomb R. T., "Methods for Reducing Aerodynamic Drag," NASA Conference Publication 2211, Proceedings of Dryden Symposium, Edwards, California, 16 September 1981.

[68] J. E. Yates, and C. Donaldson, "Fundamental Study of Drag and an Assessment of Conventional Drag-Due-To-Lift Reduction Devices," NASA Contract Rep 4004, 1986.

[69] Maughmer, M.D., "The Design of Winglets for High-Performance Sailplanes," AIAA Paper 2001-2406, June 2001.

[70] Monier Ali ElFarra, "Horizontal Axis Wind Turbine Rotor Blade Winglet And Twist Aerodynamic Design And Optimization Using CFD", Ph.D., Aerospace Engineering Department, January 2011.

[71] Thomas, F., "Fundamentals of Sailplane Design", Translated by Judah Milgram, College Park Press, MD, 1999.

[72] Falk, T.J. and Matteson, F. H., "Sailplane Aerodynamics", American Soaring Handbook, Soaring Society of America, 1971.

[73] "What is Biomimicry?" The Biomimicry Institute, Missoula, Montana.  
<http://biomimicry.org/what-isbiomimicry/>. Accessed 11/17/14.